CZECH TECHNICAL UNIVERSITY IN PRAGUE

Faculty of Nuclear Sciences and Physical Engineering

Department of Physics

Diploma Thesis

Vertex detectors for heavy flavor physics

Michal Tesař

Supervisor: Mgr. Jaroslav Bielčík, PhD.

Praha 2010

Prohlášení

Prohlašuji, že jsem svou diplomovou práci vypracoval samostatně a použil jsem podklady (literaturu, projekty, SW atd.) uvedené v přiloženém seznamu.

Nemám závažný důvod proti užití tohoto školního díla ve smyslu § 60 Zákona č.121/2000 Sb., o právu autorském, o právech souvisejících s právem autorským a o změně některých zákonů (autorský zákon).

V Praze dne 6. května 2010

Michal Tesař

Název práce:
Vertexové detektory ve fyzice těžkých kvarků

Autor: Michal Tesař

Obor: Jaderné inženýrství

Zaměření: Experimentální jaderná fyzika

Druh práce: Diplomová práce

Vedoucí: Mgr. Jaroslav Bielčík, PhD., Katedra fyziky, Fakulta jaderná a fyzikálně inženýrská, České vysoké učení technické v Praze

Abstrakt: V současnosti je připravován nový vertexový detektor Heavy Flavor Tracker (HFT) pro experiment STAR na urychlovači RHIC. Jeho úkolem je přímá topologická rekonstrukce hadronů obsahujících těžké kvarky. Provedli jsme analýzu dat simulujících nejnovější konstrukci HFT, přičemž jsme se zaměřili na maximalizaci signifikance signálu pocházejícího z D^+ mezonu v centrálních srážkách $Au + Au$ při $\sqrt{s_{NN}} = 200\ GeV$ pro nízkou příčnou hybnost (p_T) D^+ mezonů. Pro naši studii jsme použili rozpadový kanál $D^+ \rightarrow K^-\pi^+\pi^+$a získali signifikanci vyšší než 15 pro studovanou oblast $0,5 < p_T < 2,0$ GeV/c. Úvodní části této práce se zabývají fyzikou srážek těžkých iontů a fyzikou těžkých kvarků, dále jsou zde pro úplnost a srovnání uvedeny výsledky jiných analýz simulací HFT. Uvádíme též základní popis detektoru STAR.

Druhá část práce se zaobírá křemíkovými fotonásobiči. Konkrétně se zde zbýváme testy fotonásobičů pocházejících z druhé vývojové řady vyrobené ve Fyzikálním ústavu Institutu Maxe Plancka v Mnichově. Tyto fotonásobiče využívají koncept zhášecího rezistoru zabudovaného přímo v mase křemíkové desky tvořící detektor. Kromě dalších vlastností těchto zařízení, které zde taktéž uvádíme, jsme se soustředili hlavně na jejich schopnost registrovat jednotlivé fotony při pokojové teplotě. Tato vlastnost byla pozorována u menších diodových polí (19 pixelů). Pro potvrzení těchto výsledků by však bylo vhodné provést další měření.

Klíčová slova: srážky těžkých iontů, kvark-gluonové plasma, těžké kvarky, D mezon, křemíkové detektory, HFT, STAR, křemíkové fotonásobiče, detekce jednotlivých fotonů

Title:
Vertex detectors for heavy flavor physics

Author: Michal Tesař

Field of study: Nuclear Engineering

Specialization: Experimental Nuclear Physics

Sort of project: Diploma thesis

Supervisor: Mgr. Jaroslav Bielčík, PhD., Department of Physics, Faculty of Nuclear Sciences and Physical Engineering, Czech Technical University in Prague

Abstract: A new vertex detector, the Heavy Flavor Tracker (HFT), for the STAR experiment at RHIC is now in development. It is dedicated to do direct topological reconstruction of heavy flavor hadrons. We analysed simulations of the latest HFT design with primary objective to maximise significance of D^+ meson signal in central $Au + Au$ collisions at $\sqrt{s_{NN}} = 200$ GeV for low D^+ transverse momentum p_T. In our studies we utilised $D^+ \to K^- \pi^+ \pi^+$decay channel. Significance higher than 15 has been obtained for $0.5 < p_T < 2.0$ GeV/c. In introductory part of this work we give an overview of heavy ion and heavy flavor physics and show results of other HFT simulations for entireness and comparison. We also present basic description of the STAR detector.

The second part of the work deals with silicon photomultipliers (SiPM). Performance and properties of second production series of SiPM with bulk integrated quenching resistor fabricated at Max Planck Institute for Physics in Munich has been studied. Beside other parameters, which are presented in this work, we investigated SiPM capability of detecting of single photons even at room temperature. This feature has been observed only within small diode arrays (19 pixels). However, further measurements should be done to confirm these results.

Key words: heavy ion collisions, quark-gluon plasma, heavy quarks, D meson, silicon detectors, HFT, STAR, silicon photomultipliers, single photon detection

Contents

List of Figures **viii**

List of Tables **ix**

Preface **1**

1 Introduction **3**
- 1.1 Heavy ion collisions and quark-qluon plasma 3
- 1.2 QCD matter probes and signatures of QGP 4
  - 1.2.1 Flow 5
  - 1.2.2 Partonic energy loss 7
  - 1.2.3 Direct Photons 10
  - 1.2.4 Strangeness enhancement 11
- 1.3 Heavy flavor physics 12
  - 1.3.1 Total charm cross section 13
  - 1.3.2 Heavy flavor R_{AA} and v_2 14
  - 1.3.3 J/ψ suppression 16
  - 1.3.4 Beauty 18

2 The RHIC facility and the STAR detector **19**
- 2.1 The RHIC accelerator 19
- 2.2 The STAR detector 21
  - 2.2.1 Time Projection Chamber (TPC) 22
  - 2.2.2 Heavy Flavor Tracker (HFT) 23
  - 2.2.3 Barrel Electromagnetic Calorimeter (BEMC) 24
  - 2.2.4 Time of Flight (TOF) 25

3 HFT simulations **26**
- 3.1 D^0 meson 26
- 3.2 Λ_c baryon 28
- 3.3 Elliptic flow 29

4 Analysis of simulated Au+Au events at $\sqrt{s_{NN}}$ = 200 GeV **31**
- 4.1 Data set 31
- 4.2 D^+ reconstruction 31

4.3 Control plots 32
4.3.1 Reconstruction efficiency 36
4.3.2 DCA resolution 36
4.4 D^+ signal significance 39
4.4.1 Rescaling of results to 100 M events 39
4.4.2 Cut optimization 39
4.4.3 Results 40
4.5 Conclusions 44

5 Silicon Photomultiplier testing **45**
5.1 Silicon Photomultiplier 45
5.2 Layout and working principle 45
5.2.1 Avalanche photodiode 45
5.2.2 SiPM 46
5.2.3 Quenching resistor 47
5.2.4 Some important SiPM characteristics 49
5.3 Physics applications of SiPMs 50
5.4 Testing of SiPM samples 51
5.4.1 Check measurements 52
5.4.2 Response to 800 nm laser illumination 55
5.5 Conclusions 61

Summary **62**

A APS testing setup **64**

References **67**

List of Figures

1.1 QCD matter phase diagram . . . 4
1.2 Space-time evolution of heavy ion collision . . . 6
1.3 Projection of flow shapes for different v_2 values . . . 7
1.4 Transverse momentum dependence of elliptic flow for hadrons in $Au + Au$ collisions . . . 8
1.5 Nuclear modification factor of charged hadron and π^0 inclusive yields for $d + Au$ and $Au + Au$ collisions at 200 AGeV . . . 9
1.6 Di-hadron correlations in $p + p$ and central $d + Au$ and $Au + Au$ collisions at 200 AGeV . . . 10
1.7 PHENIX direct photon yield measurements . . . 12
1.8 Nuclear modification factors for hyperon and antihyperon at SPS . 13
1.9 Leading order contributions to heavy quarks production cross section . . . 13
1.10 Total charm cross section measured by STAR and PHENIX . . . 14
1.11 Nuclear modification factor for charm non-photonic electrons in $d + Au$ and $Au + Au$ collisions (STAR) . . . 15
1.12 Elliptic flow for charm non-photonic electrons in $Au+Au$ collisions (PHENIX) . . . 16
1.13 SPS measurement results of J/ψ yields normalized by Drell-Yan process . . . 17
1.14 R_{AA} for J/ψ generated in $Au + Au$ at RHIC for forward- and midrapidity . . . 18

2.1 RHIC accelerating cascade . . . 20
2.2 Perspective view of the STAR detector . . . 21
2.3 Schematic drawing of STAR's TPC . . . 22
2.4 Geometry of HFT silicon detectors . . . 23
2.5 Side view of a BEMC module . . . 25

3.1 D^0 reconstruction efficiency as a function of p_T . . . 27
3.2 D^0 signal significance as a function of p_T . . . 27
3.3 Estimated D^0 invariant mass distributions for 500 M central $Au+Au$ events . . . 28
3.4 Λ_c reconstruction efficiency as a function of p_T . . . 29

3.5 Estimated Λ_c invariant mass distributions for 500 M central Au+Au events . . . 30
3.6 Two hypothetical extremal scenarios for charm quark elliptic flow . 30

4.1 D^+ decay diagram . . . 32
4.2 D^+ distribution in p_T - η plane for Monte Carlo particles . . . 33
4.3 D^+ distribution in p_T - η plane for reconstructed particles . . . 34
4.4 D^+ distribution in p_T - φ plane for Monte Carlo particles . . . 34
4.5 D^+ distribution in p_T - φ plane for reconstructed particles . . . 35
4.6 D^+ decay length vs. D^+ momentum for Monte Carlo particles . . . 35
4.7 D^+ decay length distribution for Monte Carlo particles . . . 36
4.8 Reconstruction probability of pion and kaon tracks . . . 37
4.9 D^+ reconstruction efficiency under various conditions . . . 37
4.10 DCA resolution in $x - y$ plane for pion and kaon . . . 38
4.11 DCA resolution in z-direction for pion and kaon . . . 38
4.12 D^+ signal and background before rescaling and significance after rescaling to 100 M events. . . . 41
4.13 Expected D^+ signal for 100 M central Au+Au collisions at $\sqrt{s_{NN}} = 200$ GeV, $0.5 < \mathrm{p}_T < 1.0$ eV/c . . . 42
4.14 Expected D^+ signal for 100 M central Au+Au collisions at $\sqrt{s_{NN}} = 200$ GeV, $1.0 < \mathrm{p}_T < 1.5$ GeV/c . . . 42
4.15 Expected D^+ signal for 100 M central Au+Au collisions at $\sqrt{s_{NN}} = 200$ GeV, $1.5 < \mathrm{p}_T < 2.0$ GeV/c . . . 43

5.1 Reverse biased p-n junction. . . . 46
5.2 SiPM with polysilicon quenching resistor; scheme + photo . . . 47
5.3 Electrical schematic representing one SiPM cell. . . . 48
5.4 Schematic of SiPM wafer with integrated quenching resistor . . . 48
5.5 Schematic of wafer thinning process . . . 49
5.6 Scintillator tiles for HCAL detector . . . 51
5.7 MAGIC telescope device. . . . 52
5.8 Shapes of MPI SiPMs pixel structures . . . 52
5.9 SiPM output signal examples; good and bad signal . . . 53
5.10 Amplitude of 1 p.e. as a function of overbias voltage . . . 54
5.11 Breakdown voltage as a function of temperature . . . 55
5.12 Dark count as a function of overbias voltage . . . 56
5.13 Normalized amplitude spectra at medium laser @ various temperatures . . . 58
5.14 Normalized amplitude spectra at 273 K @ various laser levels . . . 59
5.15 Amplitude spectra at 300 K @ medium laser with multi-Gauss fit . 60
5.16 Amplitude spectra at 253 K @ medium laser with multi-Gauss fit . 60

A.1 Block scheme of readout chain for the APS . . . 64
A.2 Screenshot of readout and data-visualising software testing . . . 65
A.3 Block scheme of modules inside the master FPGA and APS . . . 66

List of Tables

2.1 Radius and hit position resolution of current HFT layers 23

3.1 Λ_c signal significance 28

4.1 Summary of used cuts and their values. 32
4.2 D^+ signal significance 44

Preface

This diploma project is devoted to modern silicon pixel detectors, which are planned to be used in future high energy physics experiments. The experimental physics programme, which is of our interest, is being conducted at large sophisticated particle accelerators and their huge and very complex particle detectors. In heavy ion collisions at ultra-relativistic energies, taking place in these experiments, new state of matter called quark-gluon plasma (QGP) is thought to be created. This medium is being detected and studied via particles escaping from the reaction point of the colliding nuclei.

One of the studied subnuclear particles are the heavy quarks and therefore heavy flavor hadrons. Due to their higher masses, they behave slightly different than the lighter quarks do. They are thought to be good probe to the hot and dense nuclear medium and hence they are a subject of systematic research to date.

To get sufficient and precise information about the high energy collision, tracks of daughter particles originating from heavy flavor hadron decays have to be reconstructed accurately. For this purpose, silicon vertex detectors are built. The attribute "vertex" arose from the objective of these devices to reconstruct vertices, i.e. points in the space, where the particles are being born or where they decay to their daughter products.

The Heavy Flavor Tracker (HFT), is now proposed to become an upgrade of inner tracking system for the STAR experiment at RHIC accelerator facility. Its main purpose is to improve capabilities of measurement of displaced vertices and do direct topological reconstruction of charm and beauty hadrons and thus study the heavy flavor quarks production in heavy ion collisions. The main physics contribution of the HFT lies in partonic energy loss and fireball thermalization determination, total charm and beauty production cross section measurements, and generally, systematic study of QGP formation and its properties.

The HFT consists of three groups of independent detector systems. Two of them are formed of two layers of different silicon strip detector. The third, and for us the most interesting one, is made of two layers of extremely thin silicon pixel detectors. This subsystem uses a new technology of monolithic active pixel sensors (APS), which are fabricated by CMOS technology and provide low power consumption, high speed, and outstanding spatial resolution. These features provide HFT for mentioned direct heavy flavor reconstruction even for low transverse momentum and they make it unique in this way.

The objective of this work was to investigate capabilities of current design of the HFT to reconstruct D^+ mesons via their hadronic decay channel $D^+ \rightarrow K^-\pi^+\pi^+$. We have studied this topic through Monte Carlo simulations. Our main aim was to maximise significance of the D^+ signal at low transverse momentum. This is presented in chapter 4.

Second and technical aim was to upgrade an experimental setup for APS testing. This setup is being built at Nuclear Physics Institute in Řež near Prague of the Academy of Sciences of the Czech Republic (NPI of ASCR). Brief overview of this is given in Appendix A. Another very promising application of silicon diode arrays based detectors are so called silicon photomultipliers (SiPM), which are currently being developed and tested at Max Planck Institute for Physics in Munich (MPI). The results, obtained during a study stay at MPI, are presented in chapter 5.

Let us now briefly describe content of the other chapters: In chapter 1 we give an introduction to heavy ion collisions physics with a focus on QGP signatures and heavy flavor physics. In chapter 2, there is a basic description of the RHIC accelerator science facility and STAR experiment for which the HFT is proposed. Simulations of the HFT performance concerning other charmed particles such as Λ_c baryon and D^0 meson are shown in chapter 3.

Chapter 1

Introduction

In this chapter we will give an overview of physics which is nowadays believed to be the most relevant in study of heavy ion collisions. These are carried out at modern experimental facilities such as CERN[1] and BNL[2] on most powerful particle accelerators like SPS[3], LHC[4] and RHIC[5]. We will be especially interested in formation of a new state of matter, the quark-gluon plasma, and quantities which provide us to study the created state of nuclear matter. In first part of this chapter we will discuss general properties of heavy ion collisions. In the second part we will show capabilities of heavy quarks of giving valuable insight into the strongly interacting matter (QCD[6] matter) evolution.

1.1 Heavy ion collisions and quark-qluon plasma

The goal of physics programme of heavy ion collisions is understanding of behavior and properties of the created QCD matter. This new phase of matter is a state where quarks and gluons are not restricted by the phenomenon of color confinement any more and they are free, is called the quark-gluon plasma (QGP). This term arose because of some similarities of QGP and plasma in atomic physics. Due to high energy density, quarks and gluons are deconfined in QGP and hence QGP is a color conducting state of quarks and gluons. It is generally thought that the early universe was in time of about $10^{-5} - 10^{-4}$ s after the big bang in the QGP state. After this period, due to the space expansion, energy density decreased enough to cross a predicted border towards hadronic gas [1, 2, 3].

In Fig. 1.1, the QCD phase diagram in therms of temperature T and baryon

---

[1] Conseil europée ne pour la recherche nucléaire

[2] Brookhaven National Laboratory

[3] Super Proton Synchrotron, (CERN), in operation since 1976, now serves as a final injector for LHC

[4] Large Hadron Collider, (CERN), started in 2008, in operation since 2010

[5] Relativistic Heavy Ion Collider, (BNL), in operation since 2000

[6] Quantum Chromodynamics - physical theory describing strong interactions

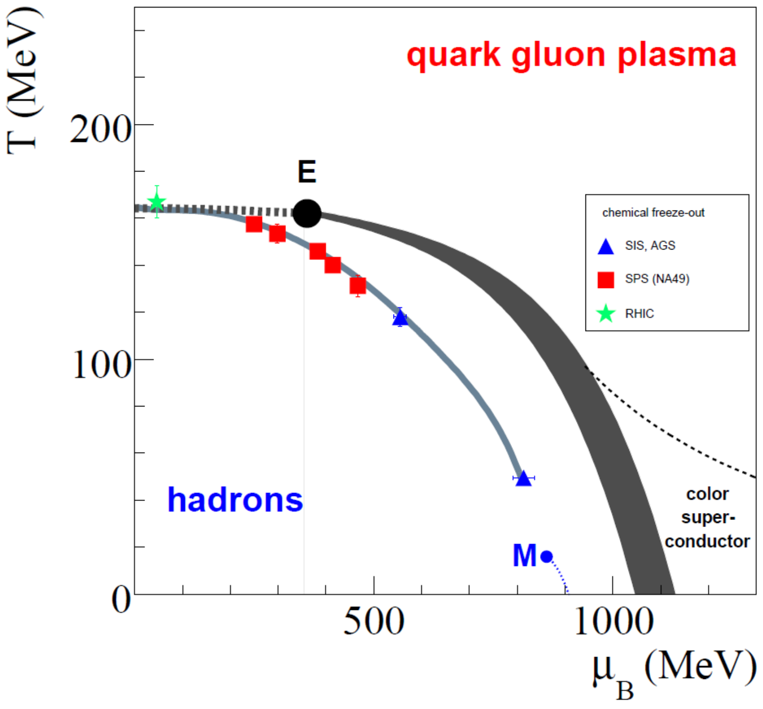

Figure 1.1: QCD matter phase diagram in the temperature T and baryon chemical potential μ_B plane. The phase transition line and the critical point E are calculated from lattice QCD. The dotted line at the bottom of the graph represents transition between hadron gas and liquid nuclear matter. This line ends with a critical point (denoted M) of nuclear matter. Taken from [4].

chemical potential μ_B[7] is shown. The dashed continuing of the phase transition curve marks a rapid and continuous cross-over transition. Lattice QCD predicts the critical temperature at low μ_B to be $T_{crit} \approx 170$ MeV $\approx 10^{12}$ K which corresponds to energy density of 1 GeV/fm^3. It is thought, that such energy density can be reached in heavy ion collisions with center-of-mass energy per nucleon pair of 10 GeV. Up to now, energies of 20 AGeV at SPS or 200 AGeV at RHIC were reached. And ultimately, LHC should provide heavy ion collisions at 5.5 ATeV in the future.

1.2 QCD matter probes and signatures of Quark-Gluon Plasma

This section deals with explaining of some of experimental observables which are believed [4, 5, 6, 7] to be to good tools to probe and study the matter created

---

[7] Chemical potential is the minimal energy necessary to add or extract a particle to or from a system. The baryon chemical potential is directly proportional to baryon number density.

in heavy ion collisions. We will also mention which experimental results could be taken as signatures of QGP formation. However, no one of them is sufficient proof of existence of QGP.

1.2.1 Flow

In a heavy ion collision, almost every created particle undergoes kind of collective motion which is called flow. While the nuclei collide with a finite impact parameter, reaction volume in not spatially isotropic as can be seen in Fig. 1.2. This spatial anisotropy will lead, due to pressure gradients in the fireball, to anisotropic momentum distribution of the particles which head out of the reacting region. The conversion takes place in early stage of the collision. During time evolution, the overlap region of colliding nuclei expands faster along its shorter axis and spatial asymmetry decreases. Consequently, momentum anisotropy will drop as well and limit itself thereby. Important thing for physical description of this situation is the reaction plane. It is defined as a plane where the impact parameter b lies. Quantitatively this phenomenon can be characterised by expanding a triple differential distribution for current hadron specie into Fourier series in azimuthal angle φ,

$$\frac{d^3N(b)}{p_T dp_T dy d\varphi} = \frac{1}{2\pi}\frac{N^2(b)}{p_T dp_T dy}\left(1 + 2\sum_{i=1}^{+\infty} v_i(p_T, b)\cos[i(\varphi - \phi_{RP})]\right) \tag{1.1}$$

where y is rapidity[8], ϕ_{RP} is azimuthal angle of the reaction plane, p_T is transverse momentum ($p_T = p_x + p_y$) and v_i are Fourier coefficients. According to this formula, we can distinguish three main kinds of flow.

Radial flow

Radial flow is represented by the first term in the parentheses in (1.1). It comports with a situation of perfectly central collision of spherically symmetric nuclei. Thus, the overlap region will be symmetric in azimuthal plane. This implies isotropic spatial distribution of particles with isotropic momentum distribution in azimuth. The other terms (however, only first two of them are really important) in (1.1) represent anisotropies of the flow and are called anisotropic flow therefore [9].

---

[8] defined by

$$y = \frac{1}{2}\ln\left(\frac{E+p_z}{E-p_z}\right) = \mathrm{argtanh}\beta,$$

where E and p_z are components of four-momentum $p^\mu = (E, p_x, p_y, p_z)$ and $\beta = \frac{v}{c}$.

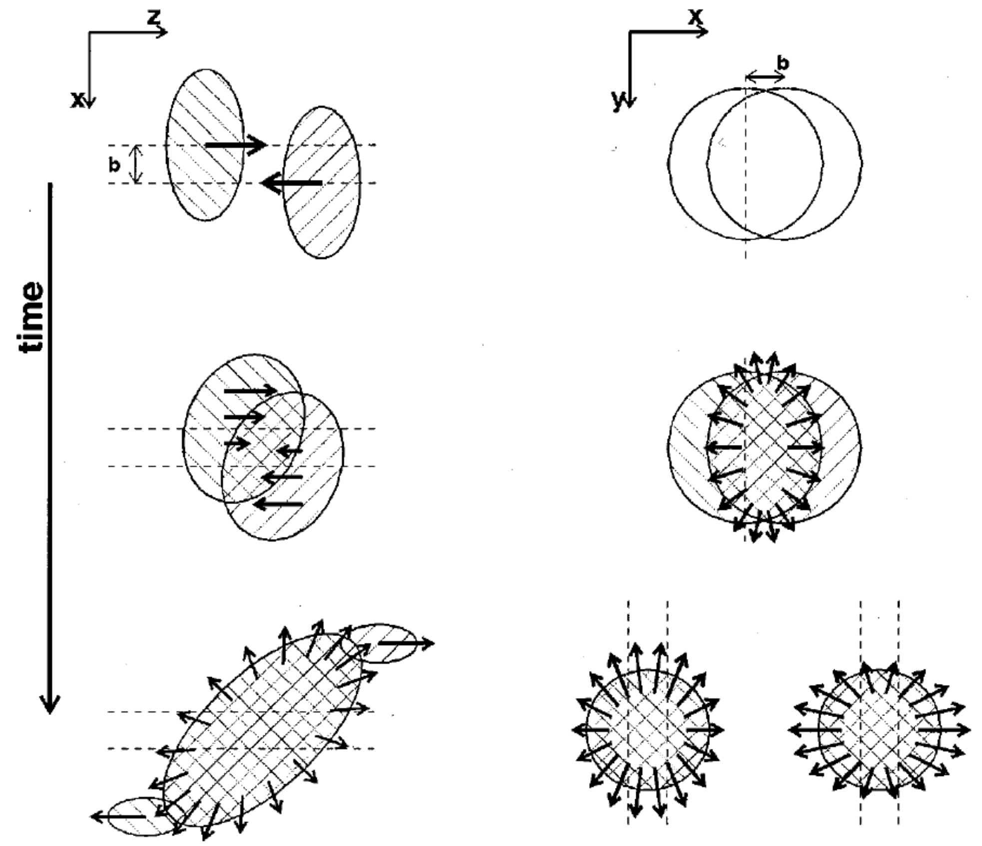

Figure 1.2: Schematic view of space-time evolution of heavy ion collision with collective motion velocity fields in $x - z$ (**left**) and $x - y$ (**right**) plane. Taken from [8].

Direct flow v_1

The first term in the sum in (1.1) quantifies emission of particles from the fireball in direction along the reaction plane. If $v_1 > 0$, it means that particles are fired out of the reaction plane in a preferential realtive angle $\Delta\varphi = \varphi - \phi_{RP} \approx 0$. Case of $v_1 < 0$ stands for emission in angle of $\sim \pi$. This phenomenon is thought to arise thanks to pressure gradients between the nuclei. The direct flow of particles originating from one nucleus is of the same magnitude but opposite direction, compared to direct flow of the second nucleus.

Elliptic flow v_2

This term has in fact four maxima of the same amplitude in $r - \varphi$ plane (r is radius) as it is obvious from (1.1) but, if added to radial flow, only two become significant (see Fig. 1.3). If $v_2 > 0$, directions of $\Delta\varphi \approx 0, \pi$ are favoured by the escaping particles. Conversely for $v_2 < 0$, preferential directions are $\Delta\varphi \approx \pi/2$ and $3\pi/2$. Anisotropic flow occurs generally only when the particles in the fireball interact among themselves often and strongly enough to transfer spatial anisotropy to momentum anisotropy. On the other hand, elliptic flow will saturate if thermalisation of the medium is set before kinetic freeze-out. Also, if collision energy is sufficiently high, elliptic flow will saturate before onset of chemical freeze-out. This allows us to study anisotropic flow of quarks themselves because their flow conserved even prior to hadronisation.

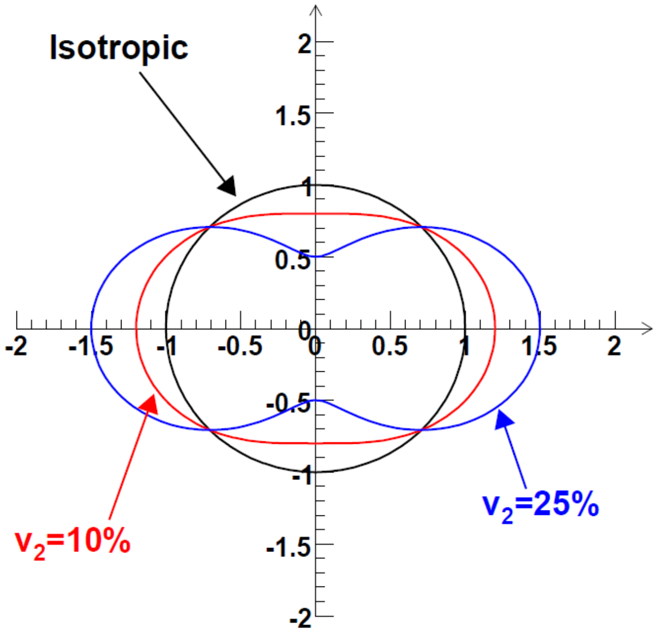

Figure 1.3: Projection of flow shapes (for different v_2 values) into plane perpendicular to reaction plane. The horizontal axis in the plot is the direction of the reaction plane. Taken from [7].

Measurements of v_2 performed at RHIC show that behavior of hadronic elliptic flow for low p_T particles correspond to an ideal fluid hydrodynamic model to a certain extent (see Fig. 1.4). Furthermore, if both axes of this plot are normalised by a number of constituent quarks of current baryons and mesons, flow of all particle species follows the same pattern. This suggests formation of elliptic flow in the phase of partonic degrees of freedom [10].

1.2.2 Partonic energy loss

Another feature of hot and dense QCD matter is the energy loss of partons propagating through this medium. If a high p_T parton, produced in primordial hard scattering, traverses medium of color charges, it will lose its energy through emission of gluons [5, 6, 11]. This is called gluonic bremsstrahlung because of similarity to photonic bremsstrahlung in electrodynamics. Energy loss of a parton per unit length (dE/dx) is believed to be sensitive to characteristic medium

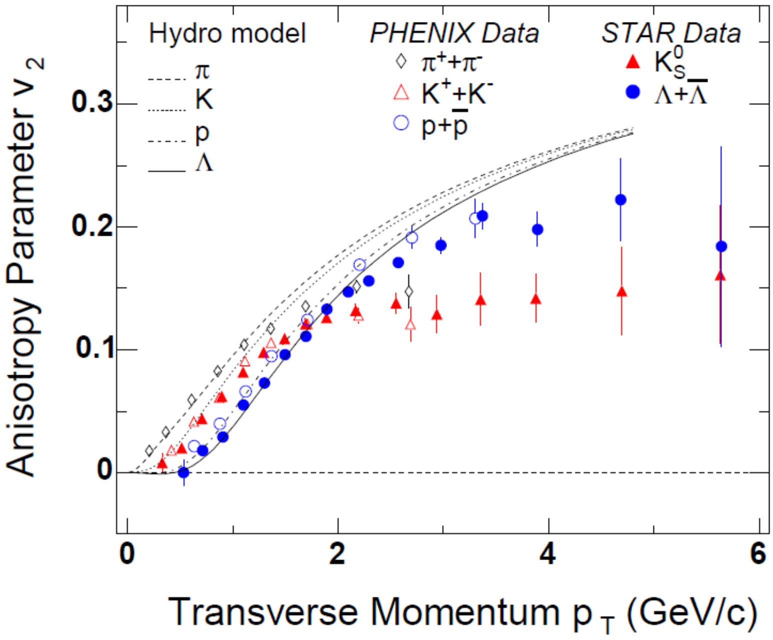

Figure 1.4: Transverse momentum dependence of elliptic flow v_2 for mesons and baryons in $Au + Au$ collisions at $\sqrt{s_{NN}} = 200$ GeV. The hydrodynamic model describes the mass dependence at $p_T < 2$GeV/c. Taken from [4].

properties such as spatial density of color charges or momentum transfer per unit length. The main difference between gluonic and photonic bremsstrahlung lies in capability of emitted gluon to interact strongly with the medium further because gluon carries color charge as well. The subsequent interactions of the gluon influence the probability of emission of the gluon itself. In theory, this leads to quadratic dependence of dE/dx on path length, contrary to quantum electrodynamics (QED), where the relation is linear. These effects enable us to use high p_T partons created in early stages of the collision as a tracer particle which probes the medium as it crosses it.

Main quantity which is used for studying effects concerning partonic energy loss is the nuclear modification factor R_{AB}. R_{AB} characterises how a spectrum of a particle is influenced by the medium. It is defined as a yield of current particle in nucleus-nucleus ($A + B$) collision N_{AB} divided by yield of the particle in $p + p$ collision N_{pp} at same energy per nucleon pair and normalised by number of binary nucleon-nucleon collisions N_{coll},

$$R_{AB}(p_T, y) = \frac{d^2N_{AB}/dp_Tdy}{N_{coll}d^2N_{pp}/dp_Tdy} \, . \tag{1.2}$$

If we talk about collision of two identical nuclei, we denote nuclear modification factor R_{AA}. In next two paragraphs we will discuss briefly some impacts of above mentioned processes.

High p_T hadron suppression

Measurements of R_{AB} of inclusive charged hadron yields done in $d + Au$ and $Au + Au$ collisions at RHIC at energy of 200 AGeV exhibit a phenomenon of suppression of high p_T hadrons up to factor of 5. If there was no influence of the medium, R_{AA} should increase with growing number of participants in the collision and at some point saturate at $R_{AA} = 1$. In central $Au + Au$ collisions at $p_T > 6$ GeV/c, we obtain $R_{AA} \approx 0.2$, which witnesses high p_T suppression (see Fig. 1.5). However, in $d + Au$ collisions no such suppression has been detected. Furthermore we observe $R_{AA} > 1$ due to Cronin enhancement [12] for $p_T > 2$ GeV/c in $d+Au$. This difference between $d+Au$ and $Au+Au$ collisions indicates that high p_T hardon suppression in not an initial state effect. It is generally interpreted as a consequence of energy loss of high momentum partons in the created nuclear medium.

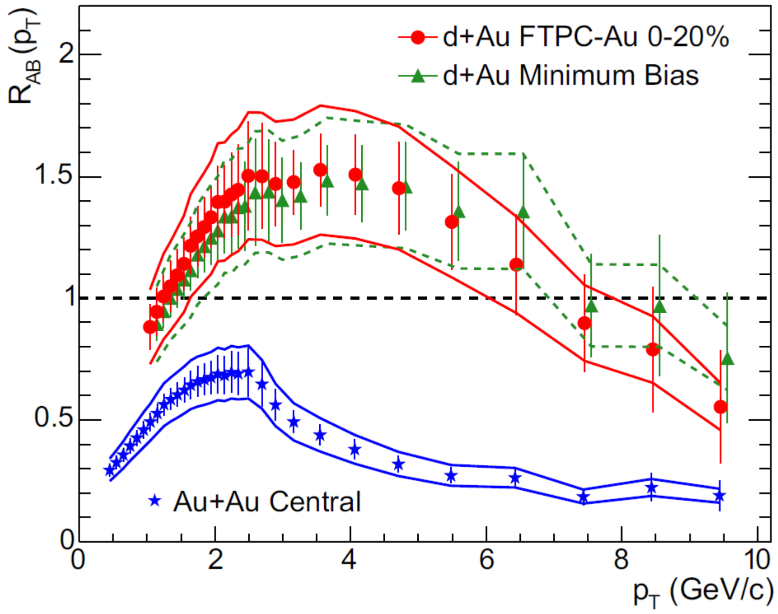

Figure 1.5: Nuclear modification factor of charged hadron and π^0 inclusive yields for $d + Au$ and $Au + Au$ collisions at 200 AGeV from STAR. Taken from [6].

Di-jet attenuation

At today maximum reachable energies in heavy ion collisions (RHIC), transverse energy[9] E_T of a jet is between 15 and 25 GeV. After hadronization the jet involves only few particles with $2 \leq E_T \leq 15$ GeV. Due to high background, jet cone analysis is difficult in this case. Experiments at RHIC use azimuthal correlation

---

[9] defined $E_T = E\sin(\theta)$ where E is total jet energy and θ is angle between beam direction and direction of the jet

of high p_T hadrons belonging to a di-jet for the analysis mainly. If so called high p_T leading particle which determines the near-side jet is chosen, the away-side jet is expected to be found in the opposite direction in relation to the leading particle. In other words, if the direction of the near-side peak defines relative azimuthal angle $\varphi_R = 0$, away-side peak should occur at $\varphi_R \approx \pi$. As can be seen in Fig. 1.6, azimuthal distribution in the away-side is slightly broadened [13]. According to high trigger for leading particle p_T, this particle originates from near surface points in the fireball. Because the other parton which generates the away-side jet, is generated in the same place as the leading one, it has to traverse almost whole diameter of the fireball. During its journey it undergoes interactions with the medium. Hence the attenuation of the away-side jet is an evidence of significance of interactions between high p_T partons and the medium. The feature of different path lengths of two particles with the same initial momentum offers more insight in the QCD matter than R_{AA} measurements.

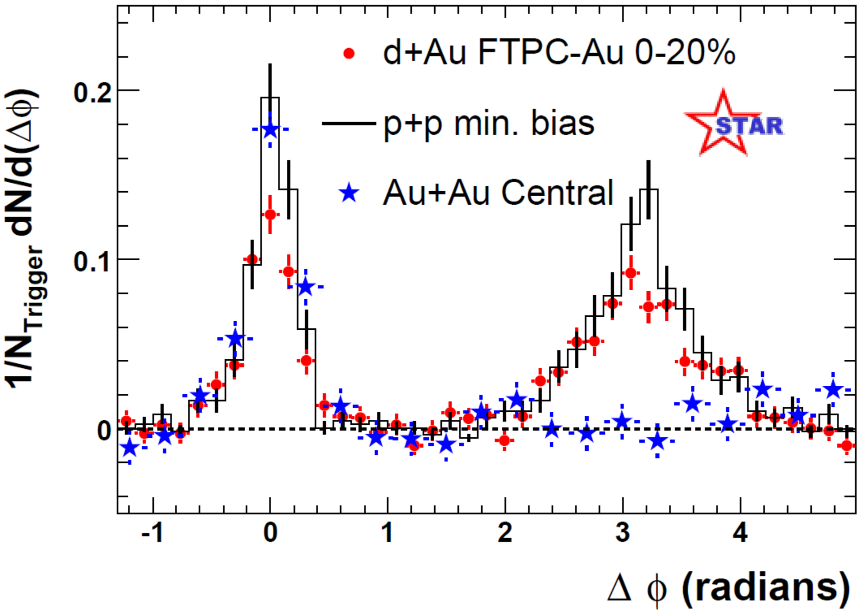

Figure 1.6: Di-hadron correlations from back-to-back di-jet production in $p + p$ and central $d + Au$ and $Au + Au$ collisions at 200 AGeV. In $Au + Au$ collisions away-side peak disappeared due to attenuation. (Trigger for leading particle: $4 < p_T < 6$ GeV/c, trigger for associated particle: $2 < p_T < 4$ GeV/c.) Taken from [6].

1.2.3 Direct Photons

Photons are produced in all stages during the QCD medium evolution. Small fraction of them (~ 2 %) is generated in very first phase of hard parton scattering. Yield of these "direct" photons decreases with growing p_T and rises with collision energy (see Fig. 1.7). An important feature which enables us to conduct these measurements is transparency of the QCD medium to these photons manifested by $R^{\gamma}_{AA} \approx 1$ [14]. However, serious problem of direct photons measurements is a huge background. This background has three sources, they take place in various time evolution stages. First component comes from electromagnetic interactions of quarks and is of energy of several GeV. The second one in generated after hadronisation and is created in hadron scattering in the medium and resonance decays. Energy range of this radiation is between few hundred MeV and few GeV. Third contribution takes place after kinetic freeze-out. Its source is mainly in resonance decays and its energy is up to few hundred MeV. These unwanted components can be determined experimentally and subtracted from the total photon production in order to separate the direct photons. Study of direct photons is important because, in fact, they come from QGP black body radiation between QGP critical temperature and temperature of about 250 MeV. Correlations of direct photons and hadrons can be utilised in further research as well.

1.2.4 Strangeness enhancement

Next signature of QGP formation is modification of strange hadron multiplicities [15, 16, 17]. Concretely, enhancement of all strange hadron species in heavy ion collisions, by factor from 2 to 20, if compared to production in $p + p$ or $e^+ + e^-$ reactions at the same binary collision energy, has been observed. This phenomenon can be seen in Fig. 1.8, where nuclear modification factor R_{AA} for strange hyperons and their appropriate antiparticles is shown. Due to some theoretical reasons [4] it is said, that in fact strangeness suppression occurs in $p+p$ and hence the strangeness enhancement also can be referred to as strangeness saturation. Furthermore, R_{AA} increases with strangeness number s of current hadrons specie., $R^{s=1}_{AA} < R^{s=2}_{AA} < R^{s=3}_{AA}$. As seen in Fig. 1.8, for Λ $R^{s=1}_{AA} \approx 2.2$ at ≥ 10 AGeV, for Ω it rises to $R^{s=3}_{AA} \approx 10$.

Strangeness enhancement can be explained in the following way. In a $p + p$ collisions, the created fireball is of small volume and the law of conservation of quantum numbers will affect the final state. Hence, the requirement of zero strangeness for the whole fireball will lead to the suppression. Conversely, in heavy ion collisions, with much greater fireball dimensions, this coherent volume has to fulfil the same restrictions as the small one and stay globally strangeness-neutral, too. However, locally can be this equilibrium broken and more s and $\bar{s}$ quarks can be produced. This also explains larger enhancement of multi-strange particles because they are now more likely to arise in a strangeness rich medium. We should also note that the experimental results are in good agreement with theoretical predictions. However, strangeness enhancement has been observed at SPS as well, where the energy is not sufficient for creation of QGP. Therefore further effects have to be taken in account, while determining total amount of produced strangeness in heavy ion collisions. Another important

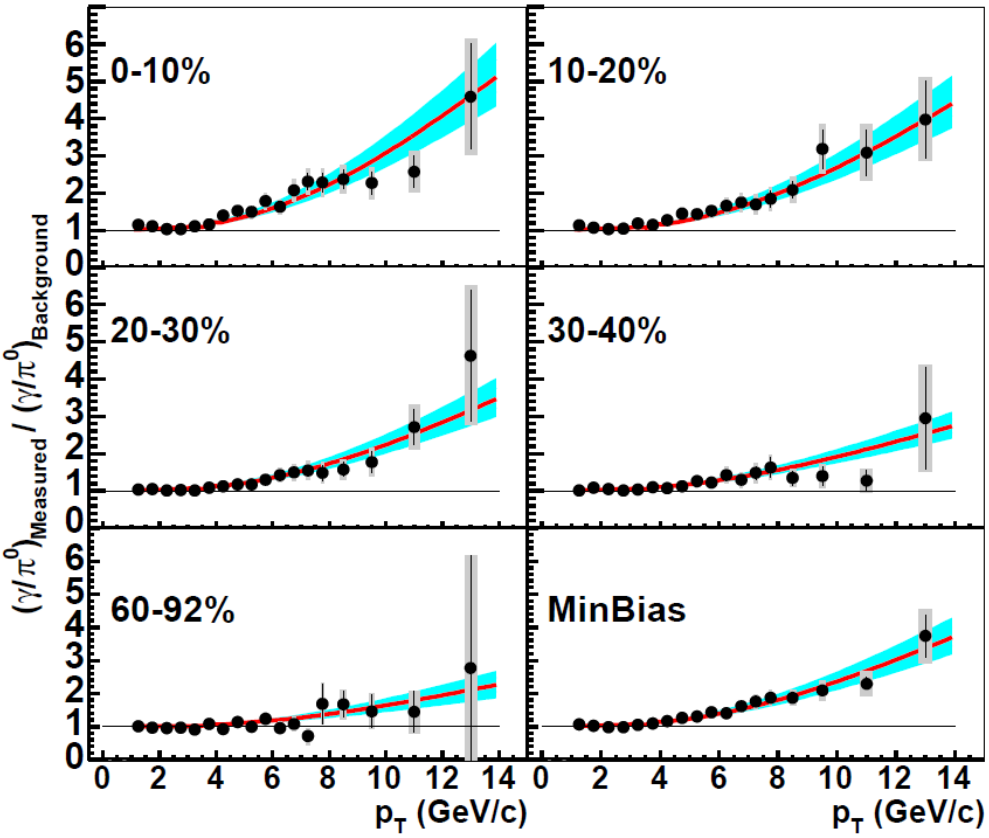

Figure 1.7: PHENIX direct photon measurements relative to the background for minimum bias and for five centralities of $Au+Au$ collisions at $\sqrt{s_{NN}} = 200$ GeV. (0-10% is the most central). The curves with the bands represent a pQCD calculation of direct photons in $p + p$ collisions with their variations for different p_T scale changes, respectively. Taken from [5].

QGP signature, the J/ψ suppression, will be discussed within following heavy flavor physics section, concretely see Sec. 1.3.3.

1.3 Heavy flavor physics

Heavy quarks[10] c and b can be produced in two following processes. A $c\bar{c}$ or $b\bar{b}$ pair can be created in a quark-antiquark ($q\bar{q}$) anihilation forming gluon which decays to a $q\bar{q}$ pair afterwards (see Fig. 1.9a). The second and the most important mechanism is gluon fusion (see Fig. 1.9b-d). Because of much higher mass of the heavy quarks, compared to the light ones, they are predicted to lose less energy via QCD bremsstrahlung, in the same way as light particles do via QED bremsstrahlung. This is why they are thought to exhibit different

---

[10] $m_{charm} = 1,25 \pm 0,09$ GeV/c^2, $m_{bottom} = 4,20 \pm 0,07$ GeV/c^2, [18]

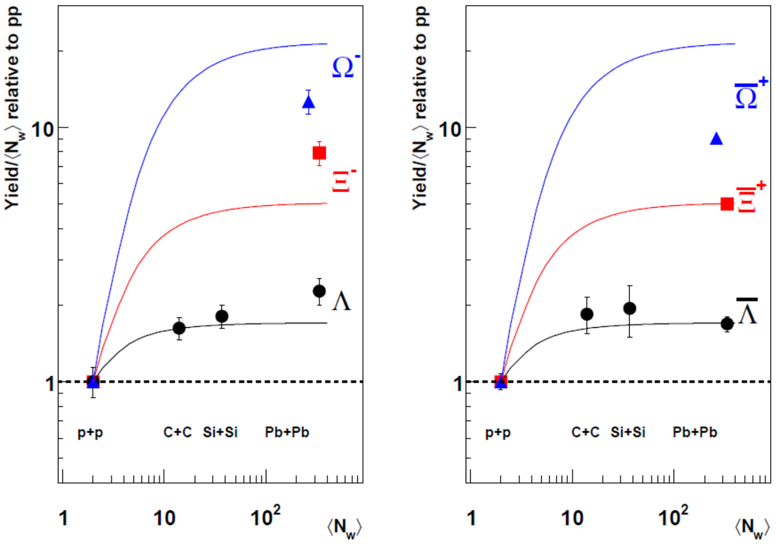

Figure 1.8: Nuclear modification factors $R_{AA}^{s=1,2,3}$ for hyperon and antihyperon production in nucleus-nucleus collisions at $\sqrt{s_{NN}} = 17.3$ GeV (SPS). Taken from [4].

energy loss patterns. However, these differences have not been observed to date. Furthermore, heavy quarks, due to their masses, are expected to arise in primordial stages of high energy particles collision. Hence, heavy quarks could serve as a good probe to early phases of the collision.

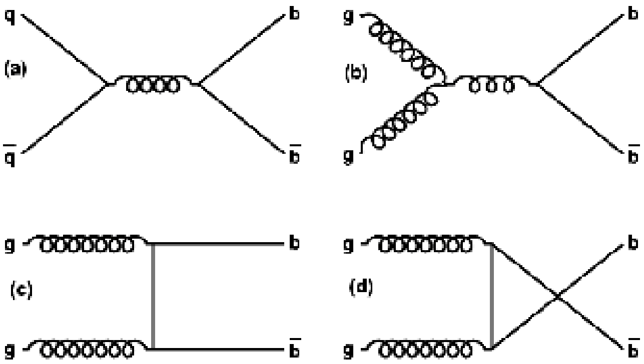

Figure 1.9: Leading order contributions to heavy quark production cross section. Taken from [19].

1.3.1 Total charm cross section

The total charm cross section [20] is very important quantity to know, especially due to testing models of J/ψ suppression (see Sec. 1.3.3). Measurements of the cross section have been done by STAR in $d + Au$ and $Au + Au$ and by PHENIX in

$p+p$ and $Au+Au$ collisions at energy of 200 AGeV. PHENIX used for the analysis non-photonic electrons (decay channel $D^0 \rightarrow K^- e^+ \nu_e$) [21] while STAR performed also direct reconstruction of D^0 mesons (decay channel $D^0 \rightarrow K^- \pi^+$) [22, 23]. Results of these analyses are summarised in Fig. 1.10. Here can be clearly seen consistency of data coming from the same experiment within different colliding systems. On the other hand, there is a discrepancy of factor ~ 2 between STAR and PHENIX. This disagreement will be a subject of further studies. Serious problem of these measurements is the inaccuracy caused by large background and statistical uncertainties. Furthermore, experimental data have to be extrapolated to low p_T where major contribution lies. For this purpose, new high precision vertex detectors are proposed at both experiments (see Sec. 2.2.2).

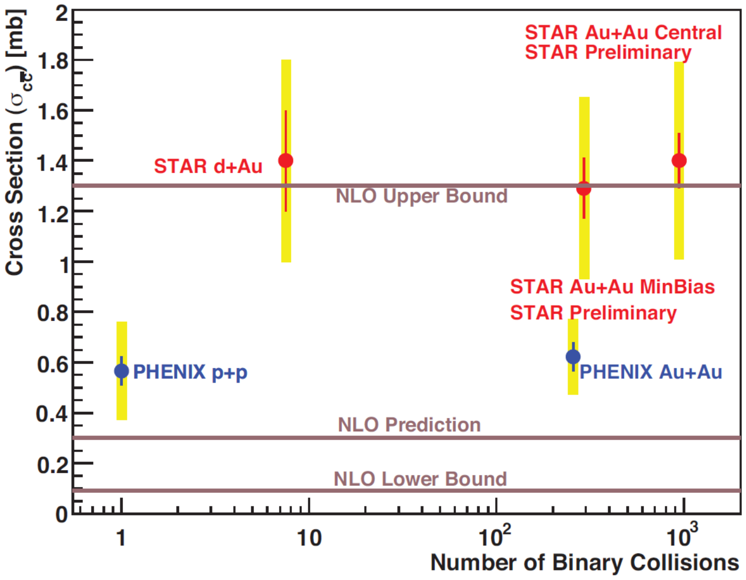

Figure 1.10: Total charm cross section measured by STAR and PHENIX. Taken from [8].

1.3.2 Heavy flavor R_{AA} and v_2

As mentioned in Sec. 1.2.2 nuclear modification factor R_{AA} and elliptic flow v_2 carries an information about energy loss of current particle specie in the nuclear medium. Both quantities have been measured at RHIC through non-photonic electrons originating from semileptonic decays of open heavy flavor mesons. Unwelcome issue of these measurements is major difficulty to distinguish charm and beauty contributions among many sources of present electrons. In Fig. 1.11 one can see experimental results obtained by STAR. Theoretical predictions suppose heavy quarks to have smaller energy loss when propagating through the QCD medium due to "dead cone" effect[11] [24]. Due to this effect, R_{AA} for beauty

---

[11] gluon radiation is suppressed at angles $\Theta < M_Q/E$, M_Q - quark mass, E - quark energy

is generally larger than for charm [25, 26]. However, in the plot is seen that heavy quarks suffer from significant energy loss leading to $R_{AA} \approx 0.2 - 0.3$ which is about the same as for light quarks.

However, in measurements of charm and beauty through non-photonic electrons, there is still a problem of resolving the particle, from which the electrons originate. Theoretical calculations of fractions of non-photonic electrons arising from charm and beauty suffer from large uncertainties. Other way to detect D and B mesons is through semileptonic decays. Within these measurements appears a problem of incomplete kinematic information about parent particle because it is taken away by escaping neutrino. Another attempt of STAR and PHENIX was to separate charm from beauty in $p + p$ collisions through electron-hadron correlations. Unfortunately, this approach suffers from poor statistics. Mentioned detection problems are intended to be solved by installing new precious vertex detectors at STAR and PHENIX, which will provide direct topological reconstruction of charm and beauty hadrons through their hadronic decays (if present for current particle specie). This upgrade will enhance signal significance of current particle specie considerably (see Ch. 3 and Sec. 4.4).

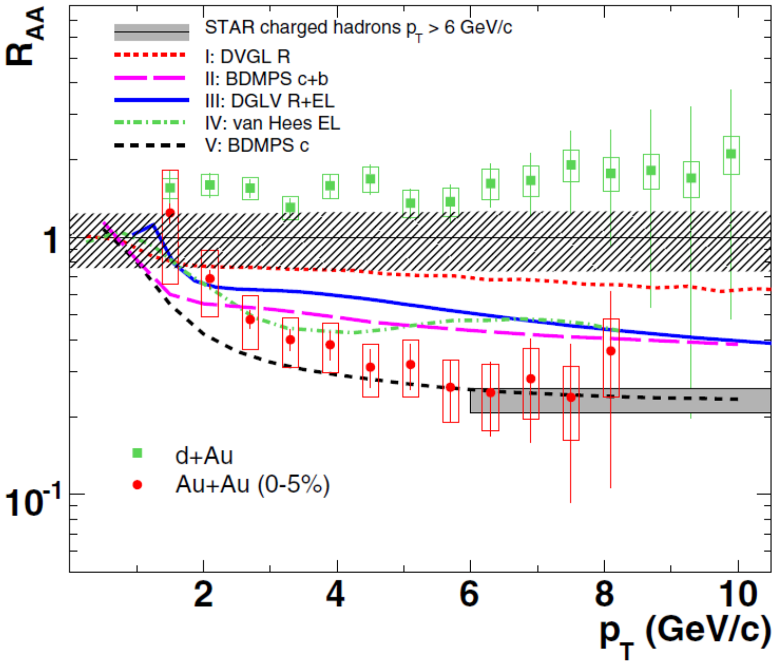

Figure 1.11: Measurements of nuclear modification factor R_{AA} in $d + Au$ and $Au + Au$ collisions at $\sqrt{s_{NN}} = 200$ GeV for non-photonic electrons (STAR). Major issue of this measurement is problematic separation of charm and beauty. Taken from [27].

Another plot, Fig. 1.12, shows elliptic flow measurements done by PHENIX. Within $p_T < 2.5$ GeV, the results signalise often interactions and thermalisation of charm quarks with the medium and hence large v_2. At $p_T > 2.5$ GeV the data exhibit large uncertainties and beauty contamination as well, therefore we cannot voice a clear conclusion about v_2 for charm quarks. Future accurate measurement will hopefully shed more light on this issue.

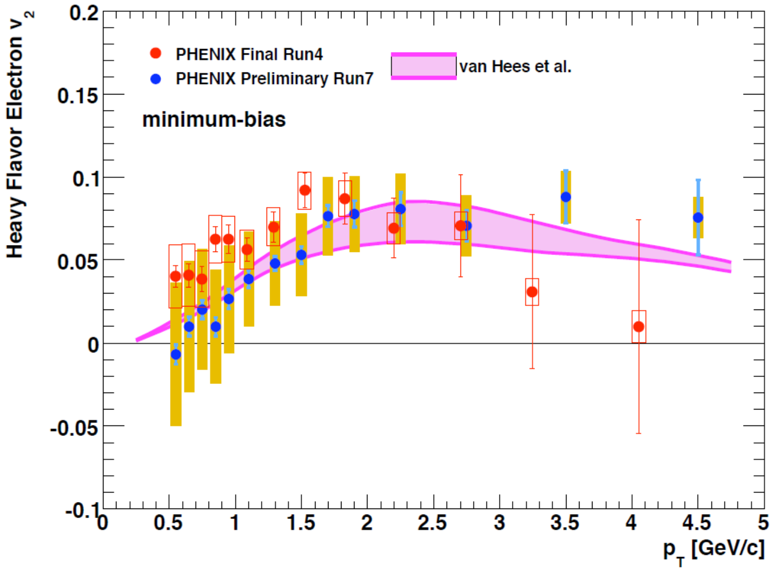

Figure 1.12: Measurements of elliptic flow v_2 in minimum bias $Au + Au$ collisions for non-photonic electrons (PHENIX), compared to theoretical predictions. Taken from [28].

1.3.3 J/ψ suppression

It turns out that heavy quarkonia, i.e. J/ψ ($c\bar{c}$) and Υ ($b\bar{b}$), yields in heavy ion collisions can be significantly changed in comparison with proton-proton or proton-nucleus collisions if QGP is formed. It has been already discovered that there are some more distinct processes which lead to J/ψ suppression even if QGP is not present. One of these so called cold nuclear matter (CNM) effects is J/ψ absorption by nuclear fragments originating from the colliding nuclei. When a J/ψ meson is created in a primordial phase of the collision, in hard parton processes, e.g. at the point where the nuclei touch each other for the very first time, the meson has to traverse the rest bulk of the nucleus. It has been discovered that this kind of suppression is exponentially dependent on path length traversed through the nucleus (so called nuclear thickness L). Parameters of the exponential law were measured at SPS NA50 experiment [29].

The second CNM effect arises because of depletion of partons with low momentum fraction x within bound nucleon compared to free nucleons. Mechanism of this effect is rather complicated. With decreasing x, gluon density rises [30]. However, maximal resolution of a number of single gluon charges is limited by momentum Q^2 transferred in the collision. These two facts lead to so called gluon saturation [4] which occurs, when the gluon density exceeds the highest possible resolution. The saturation is even greater for heavy nuclei where, because of higher nucleon density, gluon density per unit transverse area is enhanced as well. At high energies, J/ψ is generated in gluon fusion predominantly and that is why the J/ψ production is significantly influenced by mentioned effects of gluon saturation. The gluon saturation becomes important for $x \lesssim 0.05$. SPS measurement results of J/ψ yields affected by CNM effects only are shown in Fig. 1.13.

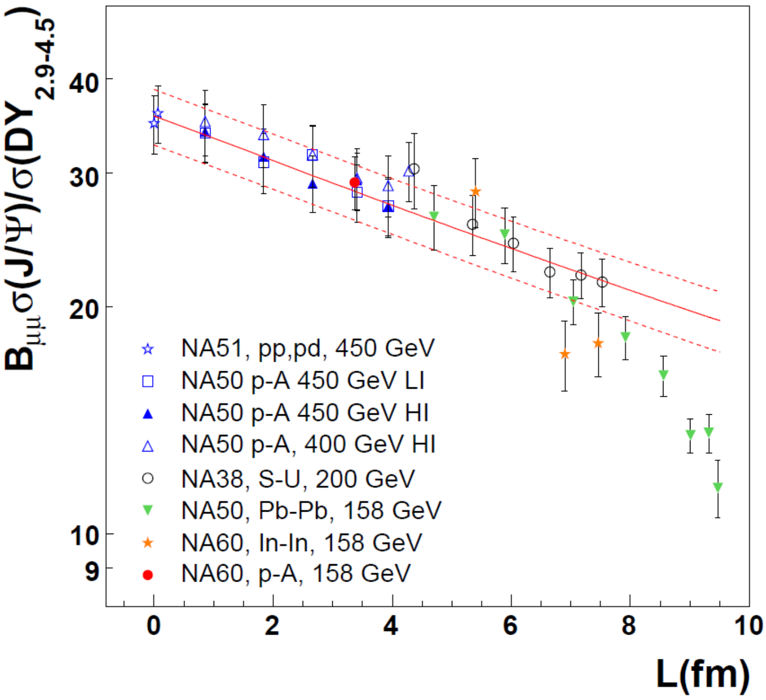

Figure 1.13: SPS measurement results of J/ψ yields normalized by Drell-Yan process [31] cross section as a function of nuclear thickness L. J/ψ detected through dimuon decay channel. Taken from [32].

If these two CNM effects are taken into account, they describe J/ψ production in proton-nucleus collisions satisfactorily. Within these collisions, there is not enough energy density to create QGP. At SPS energies, there is no anomalous J/ψ suppression present even in sulphur-uranium collisions ($A_S = 32, A_U = 238$). However, in central collisions of indium nuclei ($A = 115$), more J/ψ suppression occurs. This could be perceived as a signature of J/ψ melting in QGP. If a deconfined color conducting medium is created, color charges will be screened in a similar way as electrical charges in electromagnetic plasma due to Debye screening. As a consequence, color interaction of heavy quarks is weakened. That leads to fall of binding energy of bound states and hence to suppression of quarkonium production in QGP medium. This effect is also referred to as J/ψ melting. Also, it is not completely clear whether directly produced J/ψ

or some other excited charmonium states, e.g. ψ', χ_c which would otherwise feed down to ground J/ψ state, are suppressed. Even so all these ideas and theoretical calculations do not match the experimental results obtained at RHIC precisely. This fact is illustrated at R_{AA} measurements from RHIC in Fig. 1.14. To make the theory fit to the experimental data, more effects, such as charmonium dissociation through interactions with comoving hadrons and J/ψ regeneration in hot partonic phase due to primarily uncorrelated c and $\bar{c}$ coalescence, are taken into account. Due to these discrepancies and persisting uncertainties, further investigation should be conducted.

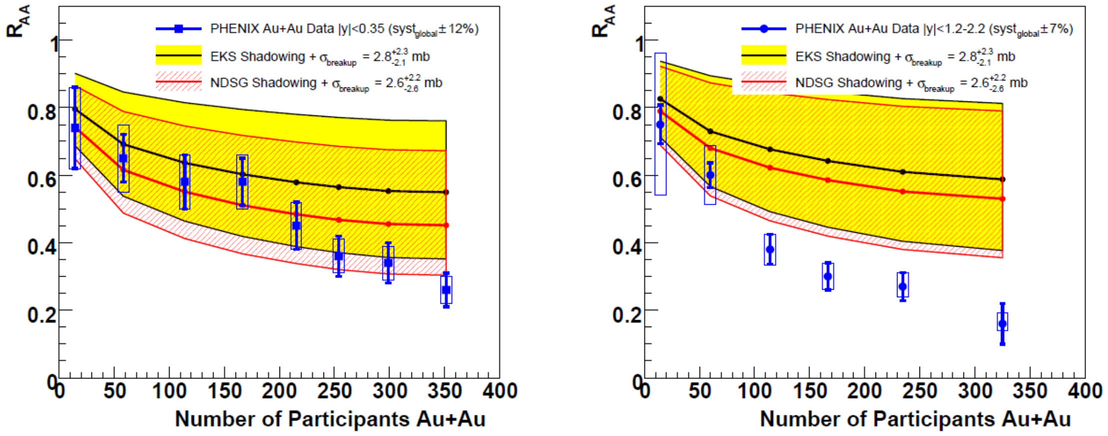

Figure 1.14: R_{AA} for J/ψ generated in $Au + Au$ at RHIC compared to theoretical curves consistent with $d + Au$ data. **Left:** At midrapidity. **Right:** At forward rapidity. Taken from [32].

1.3.4 Beauty

Physics concerning b-quark are very similar to mentioned c-quark physics modified mainly by the fact of greater b mass with all its consequences [32].

Analogous to production and suppression of charmonium is bottomium case. It is expected that understanding of effects regarding Υ could be easier than for J/ψ. The reason why, is that only few $b\bar{b}$ pairs (less than one per collision) are generated and therefore the role of regeneration is not significant any more at RHIC energies. Also because of its higher mass and hence origination from higher momentum hadrons, the effect of screening will not have such impact on bottomium production. As a next consequence of larger $\Upsilon(1S)$ binding energy, bottomium (ground state) does not suffer from the CNM breakup and the effect of melting as much as J/ψ does. However, excited states $\Upsilon(2S)$ and $\Upsilon(3S)$ are expected to melt at energies reached at RHIC. Theoretical calculations predict an upper limit of Υ $R_{AA} \approx 0.67$ at RHIC energies [33].

Chapter 2

The RHIC facility and the STAR detector

Within this chapter we will make an overview of the RHIC accelerator, where four complex detectors were placed, BRAHMS, PHENIX, PHOBOS and STAR. We will focus on STAR experiment in particular because the Heavy Flavor Tracker (HFT) detector is planned to be installed right here. RHIC, one of the world's largest and most powerful accelerators, is situated in Brookhaven National Laboratory, which is one of the biggest experimental nuclear physics facilities in the world.

2.1 The RHIC accelerator

RHIC has been in design since 1983, its construction started in 1991 and it was finished in 1999. First heavy ion collisions were performed in year 2000, and in 2001 proposed collision energy of 200 AGeV[1] in $Au + Au$ collisions was achieved.

Main objective of the RHIC project was to study nuclear matter at extremely high temperatures such as 10^{12} K, where a transition between hadronic matter and deconfined quark-gluon plasma (QGP) has been predicted. Actually, in the experimental data obtained during first three years of operation, some previously unobserved properties of matter, created in the heavy ion collisions, were detected [5]. These and the following results suggest a strongly interacting liquid medium. However, no phase transition has been observed.

The maximum design beam energies are 100 AGeV for heavy ions and 250 GeV for protons. These energies can be reached with use of following cascade of accelerators (see Fig. 2.1). RHIC has two independent ion sources and accelerating tubes, therefore it can collide two different particle species together. The first stage of accelerating procedure is Van de Graaf accelerator for heavy ions and Linac for protons. After accelerating negatively charged ions by the Van de Graaf, their electrons are partially stripped off and the ions are accelerated by Tandem to 1 AMeV. In the next stage the ions are transferred to Booster Synchrotron, where

---

[1] more precisely collision energy of 200 GeV per nucleon-nucleon pair in centre of mass system

they are accelerated to 95 AMeV. They are further ionised and injected into Alternating Gradient Synchrotron (AGS). In AGS the ions are accelerated to energy of 10.8 AGeV and stripped of remaining electrons reaching full ionisation at the exit of AGS. Thereafter, the ions are sent to main RHIC superconducting synchrotron ring of 3.8 km in circumference and brought to mentioned terminal energy of 100 AGeV. The acceleration scenario for protons, which can be polarised, differs in the fact, that the protons are injected from Linac (200 MeV) directly to Booster. Further they are accelerated in a similar way as the gold ions.

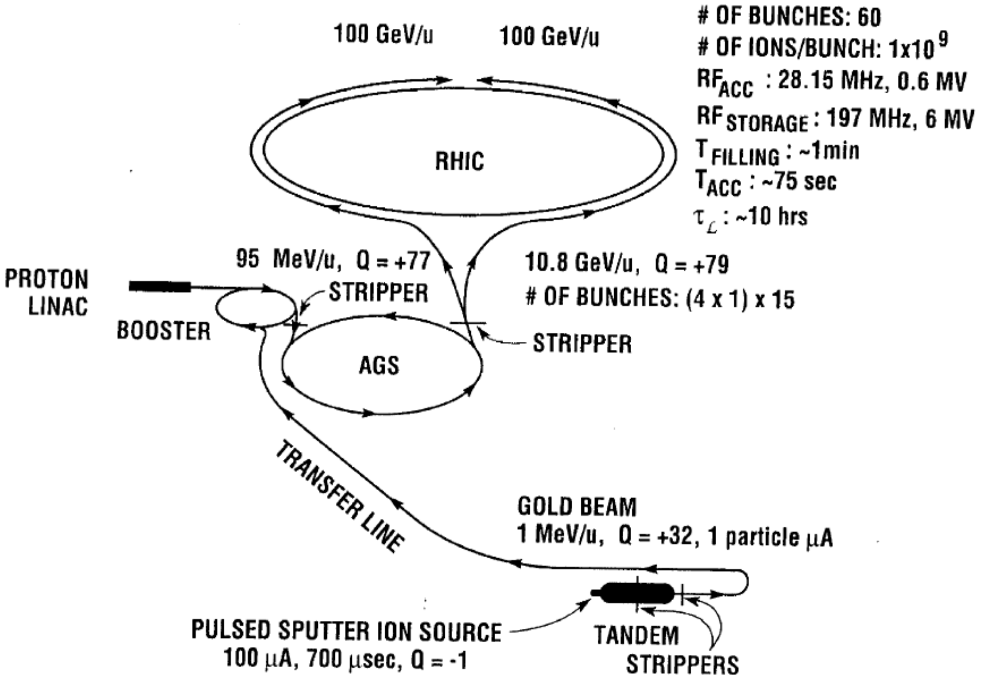

Figure 2.1: RHIC accelerating cascade. Q denotes current charge of gold ions. Taken from [34].

The two beam tubes of main the RHIC machine, where particles are revolving in opposite directions, intersect in six points. In four of them, detectors BRAHMS, PHENIX, PHOBOS and STAR are placed. PHENIX and STAR are larger than BRAHMS and PHOBOS which have already finished data taking.

The BRAHMS detector consists of a two-arm magnetic spectrometer. One is in the forward direction and is dedicated to measurements of high momentum particles within a small azimuthal angle. The other one detects particles in midrapidity region. The arms are movable and consist of narrow gap dipole magnets, drift chamber planes, Čerenkov counters, time-of-flight and tracking detectors.

The PHOBOS consists of a two-arm magnetic spectrometer and a series of ring multiplicity detectors, which provide almost 4π solid angle coverage. Additional high resolution and high speed silicon micro-strip devices provide particle detection at very high rates. For particle identification time-of-flight is used.

The PHENIX detector consists of three magnetic spectrometers, Central Spectrometer and two Muon Arms. The Central Spectrometer covers selected solid angles with quasi-concentric layers of high speed detectors of various types. The combination of these detector systems provides good tracking and particle identification. Further vertex detectors measure collision point position. This technical solution allows PHENIX to conduct very complex measurements of multiple observables.

The STAR detector will be described in the next section in detail.

2.2 The STAR detector

The Solenoidal Tracker at RHIC (STAR) [35, 36] belongs with PHENIX to the two large detectors at RHIC. STAR is a very complex device and consists of many detector subsystems (see Fig. 2.2). It has been planned and built for simultaneous measurement of many observables, which are key for studying and understanding properties of nuclear matter created in ultra-relativistic heavy ion collision. The detectors inside STAR are placed in a solenoidal coil (~ 0.5 T). They cover large solid angle and are adjusted to detect particles in high multiplicity environment (~ 1000 per unit of pseudorapidity). In the following sections we will describe the most important detector subsystems of STAR.

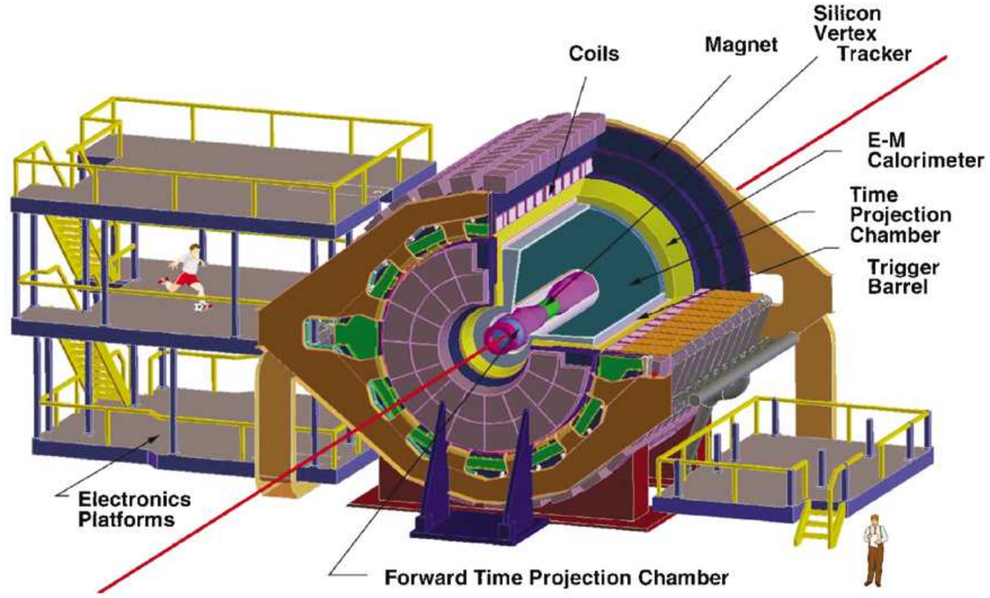

Figure 2.2: Perspective view of the STAR detector with a cutaway for viewing inner detector systems. Taken from [35].

2.2.1 Time Projection Chamber (TPC)

TPC (see Fig. 2.3) is the primary tracking detector of the STAR. It records tracks of charged particles and measures their energy loss dE/dx. From this information, particle momentum p between 100 MeV/c and 30 GeV/c and particle specie can be determined within momentum range 100 MeV/c $< p <$ 1 GeV/c. The TCP [37] covers full azimuthal angle and ±1.8 units of pseudorapidity and it is able to operate in full range of multiplicities. It is 4.2 meters long and has a diameter of 4.0 m. The inner volume is filled with gas (10% methane, 90% argon) and a uniform electric field of $\sim$ 135 V/cm is applied. This electric field is maintained by the Central Membrane operated at 28 kV, two concentric field cage cylinders and detection end-caps at zero potential.

In the end-caps, Multi-Wire Proportional Chambers (MWPC) with 45 pad rows are used for detection of electrons liberated by the ionising particle. Thanks to the electric field the electrons drift towards the end-caps, where they are registered. MWPC anode wires are of 20 μm in diameter and provide amplification between 1000 and 3000. While determining particles track, x and y coordinate of one point of the track is obtained from the end-cap MWPCs and the z coordinate is calculated from electron drift time. An interaction point, where the nuclei collide, is situated in the center of the TPC ($z = 0$), therefore particles heading out of the interaction point into front or rear hemisphere can be detected.

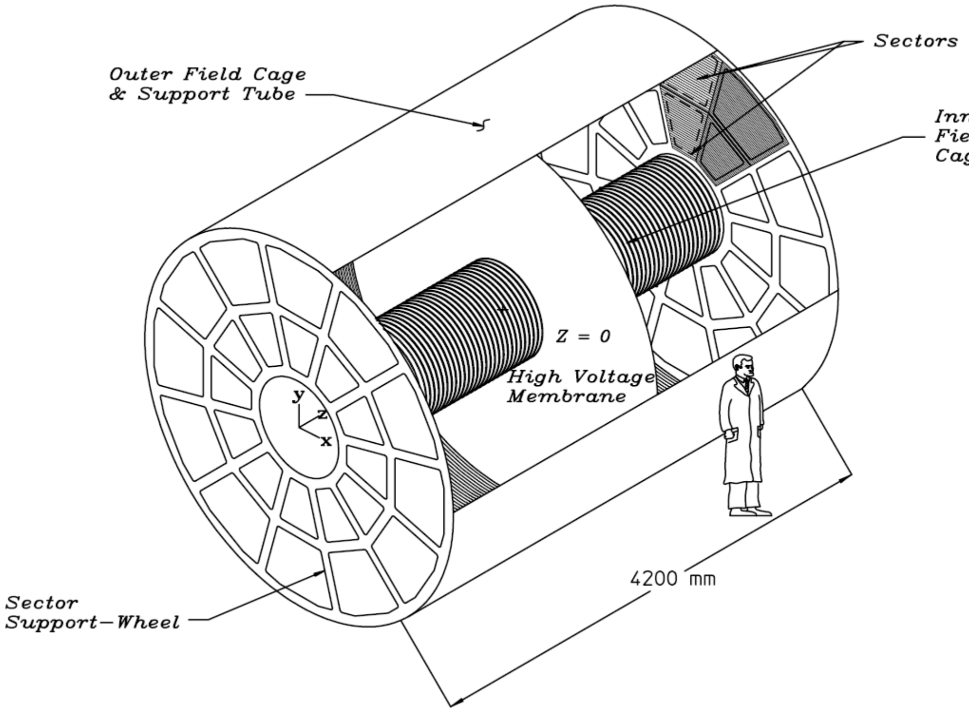

Figure 2.3: Schematic drawing of STAR TPC. Taken from [38].

2.2.2 Heavy Flavor Tracker (HFT)

The HFT detector [39, 40] is placed in the center of the TPC and together they constitute the STAR inner tracking system. It consists of three detector systems (see Fig. 2.4), while one is already installed and two are planned. HFT has 2π azimuthal and ±1.0 pseudorapidity coverage. The main purpose is further improvement of tracking accuracy and precise reconstruction of displaced vertices (secondary vertex resolution 50 μm) of heavy flavor mesons with short $c\tau$[2]. Basic properties of all HFT subsystems are summarised in tab. 2.1.

layer	r[cm]	hit resol. $(r-\phi\times z)$ [$\mu m\times\mu m$]
SSD	23	30×699
IST	14	115×2900
PXL2	8	5×5
PXL1	2.5	5×5

Table 2.1: Radius and hit position resolution of current HFT layers.

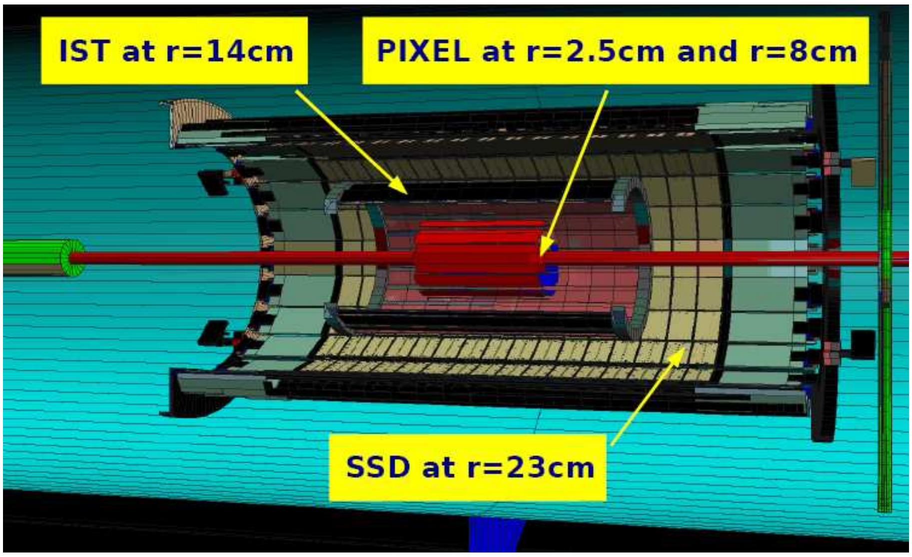

Figure 2.4: Geometry of HFT silicon detectors of the STAR inner tracking system. Taken from [40]

Pixel detector (PXL)

The high displaced vertex resolution can be achieved with use of low-mass monolithic active pixel sensors (APS) fabricated by CMOS technology. The part of the

---

[2] c - speed of light in vacuum, τ - mean lifetime of current particle specie

detector, which is built of APS, is called the pixel detector (PXL) and consists of two layers. The inner layer lies as close to the beam pipe as possible (at radius r = 2.5 cm) and is assembled of 10 ladders, while the outer one (r = 8.0 cm) is of 30 ladders (length ~ 10 cm). Each ladder is carries 10 APS chips. Pitch of the pixels will be 18.4 μm and total number of channels is planned to be ~ 436 M. PXL will cover pseudorapidity interval of ±1.2. Because of small thickness of a newly proposed beam pipe (0.15% X_0[3]) and the detector (with its support structure 0.37% X_0 per layer), production of e^+e^- pairs from photon conversions and multiple Coulomb scattering will be significantly reduced.

This detector has not been constructed yet.

Intermediate STAR Tracker (IST)

The second HFT subsystem is the IST, a single-sided fast strip detector placed at r = 14.0 cm. Its task is to improve pointing resolution of the tracks reconstructed in Time Projection Chamber (TPC) in the high-multiplicity environment of heavy ion collisions. IST will be made of 24 ladders (50 cm long) with 144 sensors and total ~ 111 K channels. Dimension of proposed strips is 600 × 6000 μm^2. Thickness of sensor wafers will be ≤ 1.5% X_0. IST preudorapidity coverage will be ±1.

This detector has not been constructed yet.

Silicon Strip Detector (SSD)

The SSD [41] is the outermost layer of the HFT. Function of the SSD is to detect particles with higher pointing resolution than TPC does and improve overall tracking capability. The SSD is placed at radius of 22 cm away from the beam line (see Fig. 2.4) and covers pseudorapidity range of ± 1.2. The detector is assembled of 10 ladders, with each ladder carrying 16 wafers using double-sided silicon strip detectors with 768 strips with pitch of 95 μm on each side. The wafers are 300 μm thick, which corresponds to 1% X_0 and the strips are oriented perpendicularly to longer detector dimension on both sides. The SSD has about 1 m^2 of sensitive surface and 500 K channels, it is cooled by flowing air and its particle detection efficiency (see Sec. 5.2.4) is 95%. This detector already exist, it is placed in the STAR and it is functional.

Previously it has been considered as an independent system, but in the latest approaches it has been comprehended to the HFT project.

2.2.3 Barrel Electromagnetic Calorimeter (BEMC)

STAR BEMC detector [42] is dedicated to trigger rare high p_T processes such as direct photons, jets and heavy flavor. It is paced outside the TPC in pseudorapidity

---

[3] X_0 - radiation length [37]

range of ±1 and extends on 60 m^2. BEMC is able to detect up to 60 GeV electromagnetic showers and its thickness is 20 X_0 at 0 pseudorapidity. The showers are created in lead convertors and detected by plastic scintillators, while the light output is amplified by classical photomultiplier tubes (PMT). The BEMC is segmented into 4800 towers and every tower is pointing to direction of interaction point (see Fig. 2.5). As it can be seen in the figure, also Shower Maximum Detectors (SMD) are implemented in the BEMC to improve electromagnetic shower spatial resolution. SMD consists of two perpendicularly oriented layers of gas wire pad chambers. Presence of the Barrel SMD is essential for π^0 identification, direct photons and W and Z decays.

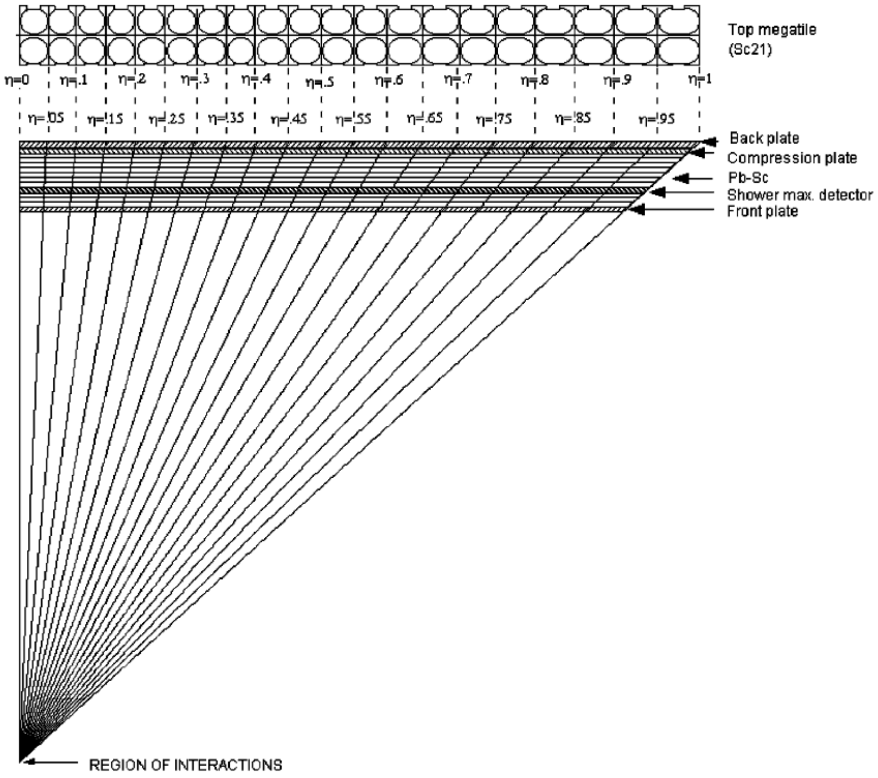

Figure 2.5: Side view of a BEMC module showing the projective nature of the towers. Taken from [42].

2.2.4 Time of Flight (TOF)

The STAR TOF detector [43, 44] has been built to extend particle identification (PID) capability of the TPC. It covers ±1 in pseudorapidity, full azimuthal angle and has detection efficiency about 95%. The TOF uses Multi-gap Resistive Plate Chambers (MRPC), which offer time resolution below 100 ps. It significantly contributed to measurements concerning charmed hadrons, non-photonic electron analysis and many others.

Chapter 3

HFT simulations

In this chapter, we will present simulations of the Heavy Flavor Tracker (HFT), which are concerned with charmed hadrons detection and study of their properties. We will be interested predominantly in signal significance[1] and detection efficiency for given particle specie. These quantities tell us about our detection capability, which is of crucial importance for all measurements. These performance tests, as well as our own analysis of D^+ meson in Ch. 4, were done for latest HFT design (see section 2.2.2). The statistical set was 10 000 central $Au+Au$ events.

3.1 D^0 meson

D^0 meson, as mentioned above, is a very helpful tool for obtaining information about total charm yield in heavy ion collisions and c-quark fragmentation function. D^0 mesons are detected through their hadronic decay channel $D^0 \to K^-\pi^+$ (B.R. = 3.8%).

In Fig. 3.1, signal reconstruction efficiency for D^0 mesons with flat and power-law p_T spectra for central $Au + Au$ collisions is shown. These values represent upper limit for real measurements. Two cases are depicted in the plot. The first one is with tracking condition applied (> 15 hits in TCP and 2 hits in PXL) and the second one represents signal after tracking and additional cuts used for background suppression. Above $p_T \approx 2$ GeV, the efficiency is about 10%, but for lower p_T it rapidly drops up to 0.1% due to multiple Coulomb scattering on beam pipe and detector support structures.

D^0 signal significance as a function of p_T for central $Au + Au$ collisions can be seen in Fig. 3.2. It shows that the HFT would be capable of measuring D^0 mesons even at low p_T such as 0.5 GeV/c.

To illustrate this, we also present what would D^0 invariant mass distribution look like for low and high p_T (Fig. 3.3). In these pictures, results obtained within

---

[1] defined as $\frac{S}{\sqrt{S+B}}$, where S - signal, B - background

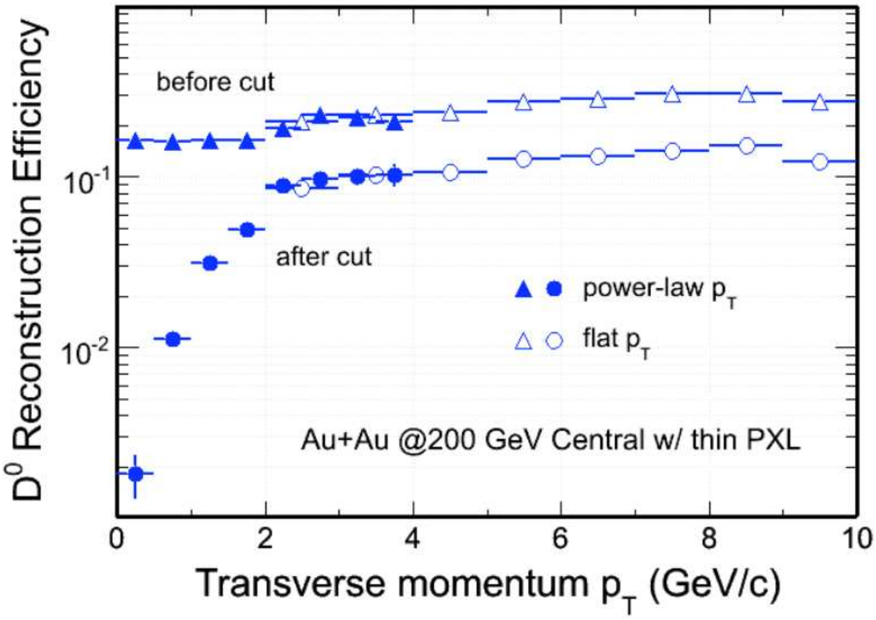

Figure 3.1: D^0 reconstruction efficiency as a function of p_T. Filled symbols are for a power-law input p_T distribution and open symbols are for a flat input distribution. Taken from [40].

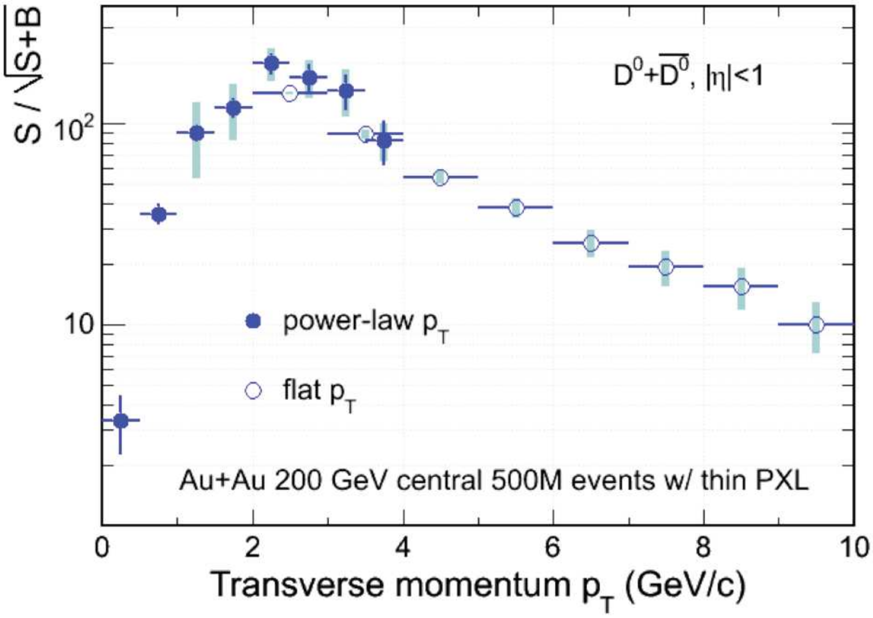

Figure 3.2: D^0 signal significance as a function of p_T. Filled symbols are for a power-law input p_T distribution and open symbols are for a flat input distribution. Taken from [40].

10 K central $Au + Au$ events were rescaled to 500 M, which will correspond to 5 months of taking data under realistic conditions.

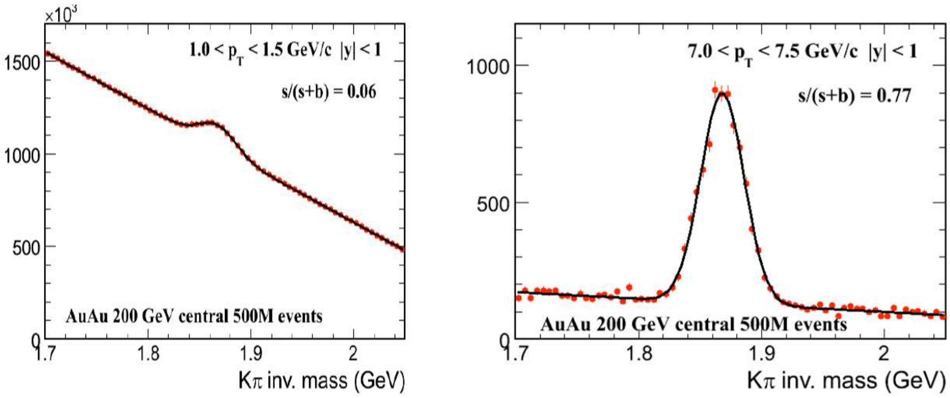

Figure 3.3: Estimated D^0 invariant mass distributions for two p_T intervals for 500 M central $Au + Au$ events. Taken from [40].

3.2 Λ_c baryon

Aside from total charm cross section determination, Λ_c baryon measurements are important due to study of baryon-to-meson enhancement ratios [45, 46]. In following simulations Λ_c baryons are reconstructed through their $\Lambda_c \rightarrow K^-\pi^+p$ decay channel (B.R. = 5.0%).

Fig. 3.4 (for Λ_c) is of the same fashion as Fig. 3.1 for D^0 mesons. It shows the reconstruction efficiency. Comparing these two plots, one can clearly see that efficiency for Λ_c is about an order of magnitude lower than for D^0. This is mainly because of its three body decay and therefore larger combinatorical background.

Tab. 3.1 shows signal significance for Λ_c at low p_T almost of two orders of magnitude lower, if compared to D^0. This is again a consequence of larger combinatorical background and multiple Coulomb scattering. One can also recognise absence of a values for lowest p_T; this is caused by difficult reconstruction and hence almost impossible significance estimation within low statistics of 10 K events.

p_T [GeV/c]	Λ_c signal significance
2 - 3	4.4
3 - 4	4.3
4 - 5	8.7

Table 3.1: Λ_c signal significance as a function of p_T. Data taken from [40].

Lastly, we present an illustrative plot (Fig. 3.5) of estimated invariant mass

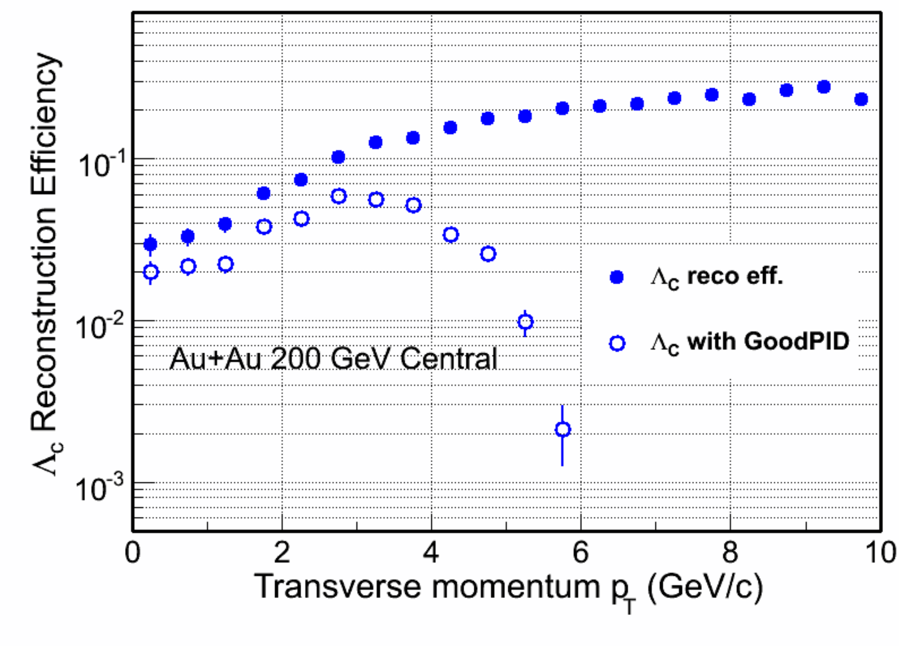

Figure 3.4: Λ_c reconstruction efficiency as a function of p_T. Filled symbols are for situation with tracking condition ony, and open symbols are for correctly identified particles without additional background suppressing cuts. Analysis done by Jan Kapitán.

distribution of Λ_c in range $3 < p_T, 4 <$ GeV/c for 500 M central $Au + Au$ collisions at 200 AGeV. It has been obtained from mentioned set of 10 K events.

3.3 Elliptic flow

Here we show a plot (Fig. 3.6), where two extremal scenarios for charm quark elliptic flow are calculated. The first one describes a situation where c-quark exhibits the same elliptic flow as light quarks do. If this was observed, it would indicate frequent interactions and thus medium thermalisation. The second slope represents hypothetical measurement of zero charm elliptic flow, which would mean low interaction rate and hence no thermalisation of the medium. This simulation has been rescaled to 500 M minimum bias $Au + Au$ collisions at RHIC energy of 200 AGeV and shows that with the HFT upgrade STAR would be able to shed light on the important issue of QCD matter thermalisation.

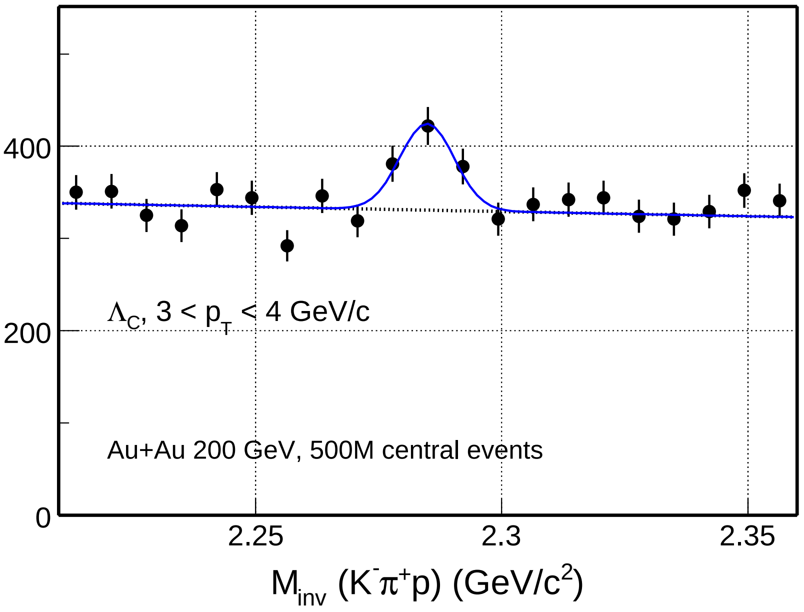

Figure 3.5: Estimated Λ_c invariant mass distributions for two p_T intervals for 500 M central $Au + Au$ events. No Λ_c enhancement assumed. Analysis done by Jan Kapitán.

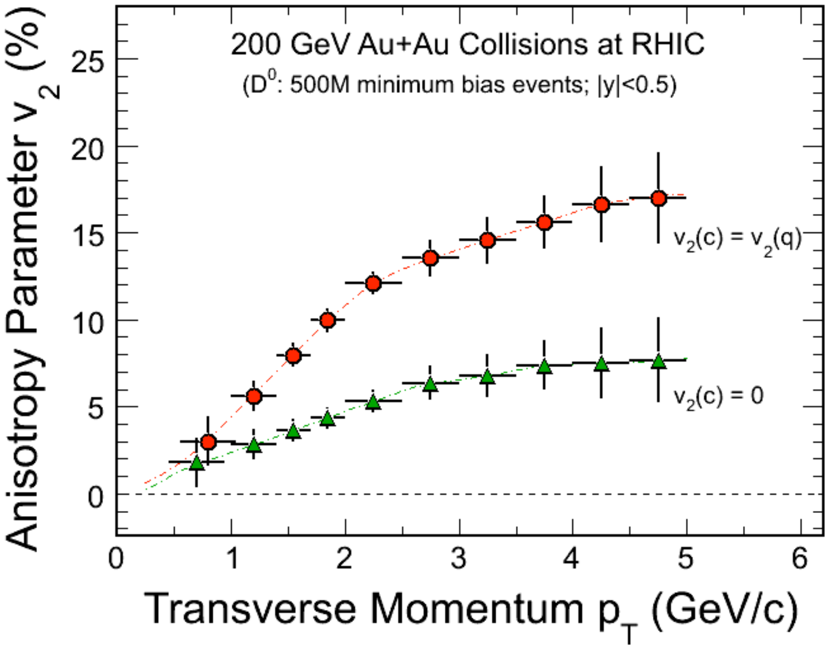

Figure 3.6: Two hypothetical extremal scenarios for charm quark elliptic flow v_2 after 5 months of data taking with the STAR HFT upgrade. One is for zero charm v_2 and the second for equal charm and light quark v_2. Taken from [40].

Chapter 4

Analysis of simulated Au+Au events at $\sqrt{s_{NN}}$ = 200 GeV

In this chapter, we will describe how a study of D^+ reconstruction capability of the HFT has been done. We will discuss our analysis methods of quantities of our interest. Further we will present the plots which probe the used simulated data set and prove its correctness. In next sections, obtained results of detectors spatial resolution and reconstruction efficiency will be shown. In the final part signal significance optimization proces and final results will be presented. This work has been done as a part of this thesis.

4.1 Data set

The data set used for analysis was 10 000 $Au + Au$ HIJING generated events. Centrality of the simulated collisions is 0 - 10 % and collision energy $\sqrt{s_{NN}}$ = 200 GeV. In each event were embedded five D^+ with flat p_T distribution from 0 to 10 GeV/c. Particles from HIJING and D^+ were filtered through GEANT model of the STAR detector with HFT upgrade ("upgr15") and detector response was simulated.

4.2 D^+ reconstruction

In the analysis we are looking for D^+ mesons [18] (1869 MeV/c^2) having $c\tau$ = 312 μm. We utilised the $D^+ \rightarrow K^-\pi^+\pi^+$(B.R. 9.5%) decay channel, hence we have to survey all possible triplets $K^-\pi^+\pi^+$. However, not all of these triplets come from D^+ decays and if we considered all the triplets, their number would be enormous. To reduce the background, we use in all analyses concerning D^+ the following set of cuts; values of some of them were further optimized (see Sec. 4.4.2). These cuts are illustrated in D^+ decay diagram (Fig. 4.1).

Distance of closest approach (DCA) of daughter particles (pions and kaons) to the primary vertex ("global DCA" cut) is desired be greater than 100 μm. On

DCA of daughters to D^+ vertex (DCA$_{V0}$) we put condition DCA$_{V0}/resolution < 2$, where *resolution* is pointing resolution for current particle specie. The pions and the kaons also have to have reconstructed hits in both PXL layers and 15 hits in TPC. Next cut is $\cos\theta > 0.99$, where θ is an angle between join of primary and secondary vertex and $K^-\pi^+\pi^+$ triplet momentum. We require the invariant mass[1] of the triplet to be between 1819 and 1919 MeV/c^2. From all the events we took only those that have the primary vertex at most 5 cm away from center of the detector in z-direction. Values of used cuts are summarised in Tab. 4.1.

quantity	range
inv. mass [MeV/c^2]	1819 - 1919
global DCA [µm]	> 100
DCA$_{V0}/resol.$	< 2
$\cos\theta$	> 0.99
vertex Z pos. [cm]	± 5

Table 4.1: Summary of used cuts and their values.

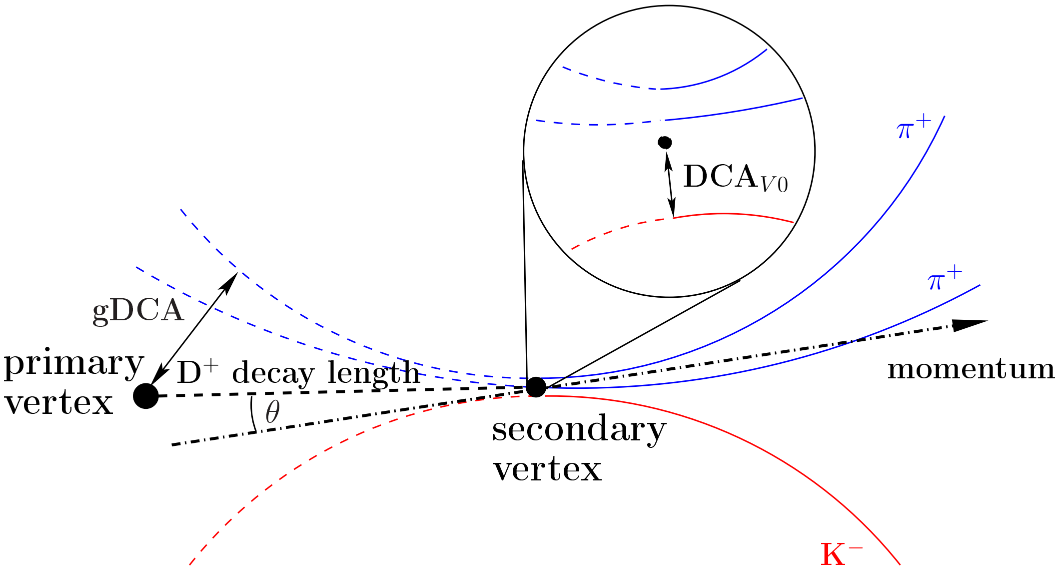

Figure 4.1: D^+ decay diagram. ($D^+ \to K^-\pi^+\pi^+$)

4.3 Control plots

To check the correctness of the data, and whether they are generated as expected, we performed a set of control plots. Fig. 4.2 shows D^+ distribution in p_T - η plane[2]

---

[1] $(M_{inv}c^2)^2 = (\sum_i E_i)^2 - \| \sum_i \vec{p_i}c \|^2$ where the sums are over all particles

[2] η - pseudorapidity, $\eta = -\ln[\tan(\theta/2)]$

for Monte Carlo (MC) simulated particles. The region $|\eta| < 1$ and $0 < p_T < 10$ GeV/c represents embedded D^+, the rest comes from HIJING. It is clear that the p_T - η distribution of embedded D^+ is flat, as it should be.

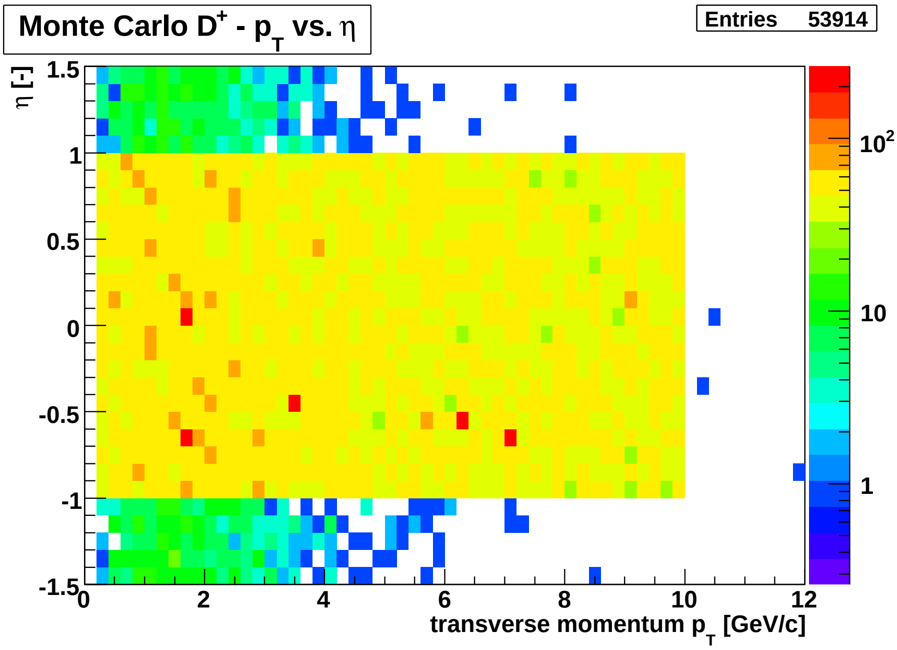

Figure 4.2: D^+ distribution in p_T - η plane for Monte Carlo particles. (No cuts applied.)

The same plot, but for the reconstructed D^+ is in Fig. 4.3. Reconstructed means that the tracks of daughter particles were correctly reconstructed by tracker. D^+ density as well as number of entries has dropped significantly and all D^+ outside the $|\eta| < 1$ region vanished due to detector acceptance. Lower density for low p_T is caused by multiple Coulomb scattering (MCS) because tracks of the scattered particles do not follow expected trajectory in magnetic field and therefore cannot be correctly reconstructed.

Very similar to the previous plots are Fig. 4.4 and Fig. 4.5 which show D^+ distribution in p_T - φ plane[3] for the Monte Carlo and reconstructed particles, respectively. In Fig. 4.4 we see that the distribution is flat too, hence the whole D^+ spatial distribution is isotropic. Higher D^+ density in low p_T region we set down to the HIJING background (in $|\eta| > 1$ region). In Fig. 4.5 this low p_T region turns into low density due to limited detector acceptance in η and MCS. In the plot for reconstructed particles number of entries falls down again.

Further we checked, if D^+ decay length as a function of momentum has correct shape (see Fig. 4.6). In this figure dependence for Monte Carlo particles (crosses) is shown. The straight line is an ideal linear function of this relation.

Next plot (Fig. 4.7) is a histogram showing distribution of decay lengths of D^+

---

[3] φ - azimuthal angle

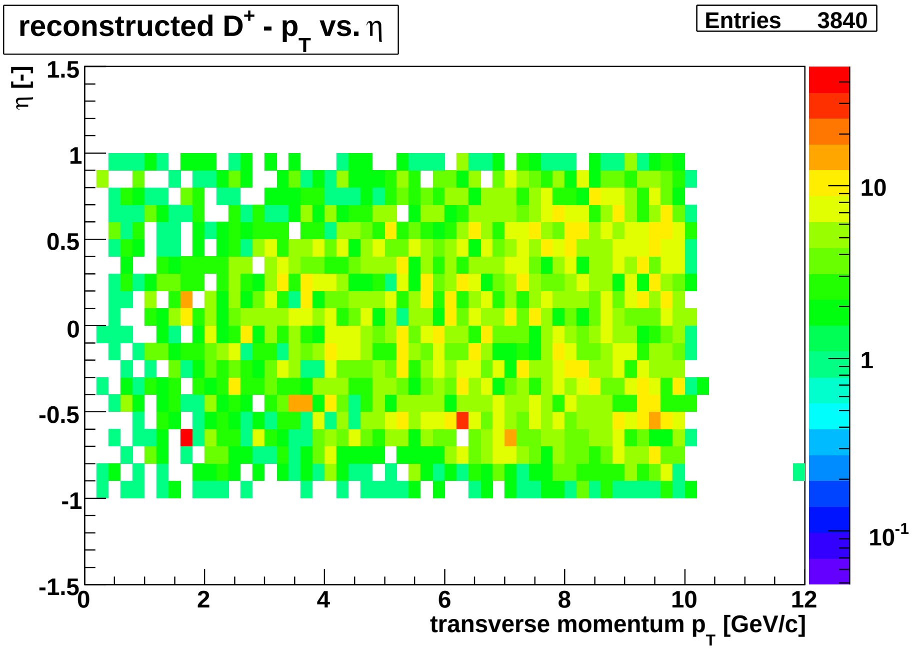

Figure 4.3: D^+ distribution in p_T - η plane for reconstructed particles.

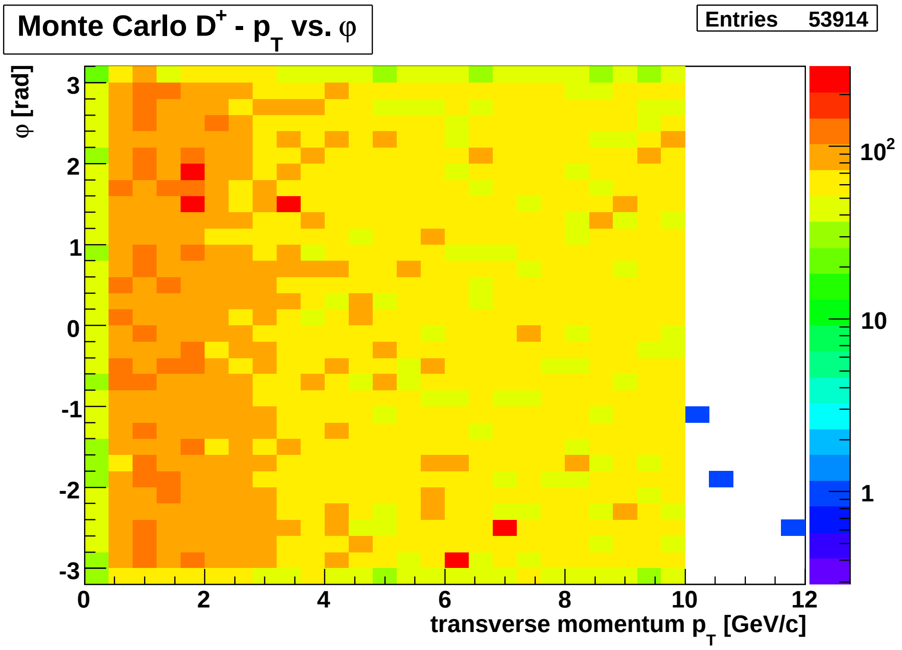

Figure 4.4: D^+ distribution in p_T - φ plane for Monte Carlo particles. (No cuts applied.)

on a logarithmic scale. It is plotted for D^+ momentum between 1 and 2 GeV/c. The relation is fitted with an exponential which describes the data well up to decay lengths of 1500 μm, where number of decaying D^+ becomes very low.

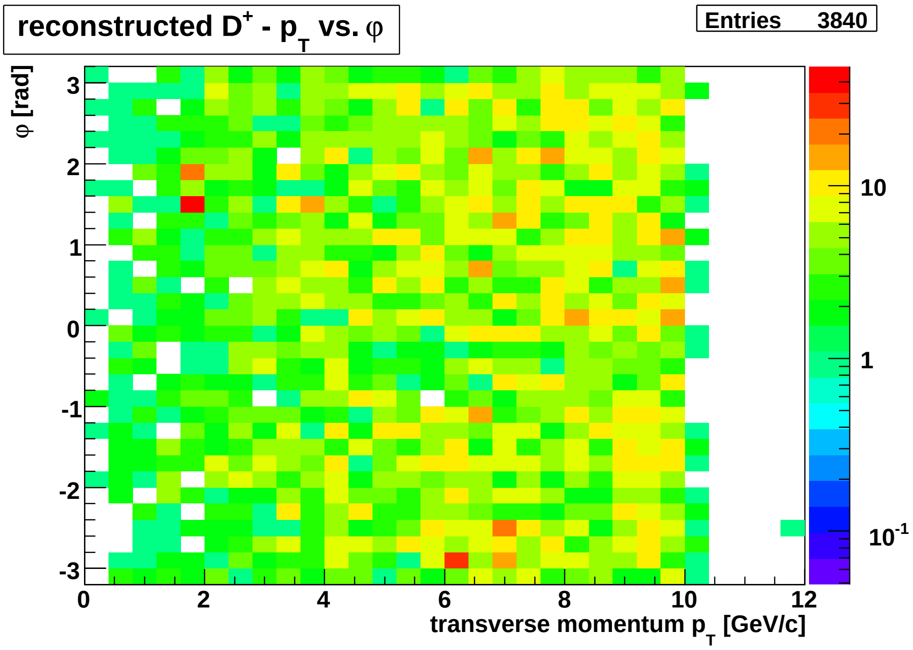

Figure 4.5: D^{+} distribution in p_T - φ plane for reconstructed particles.

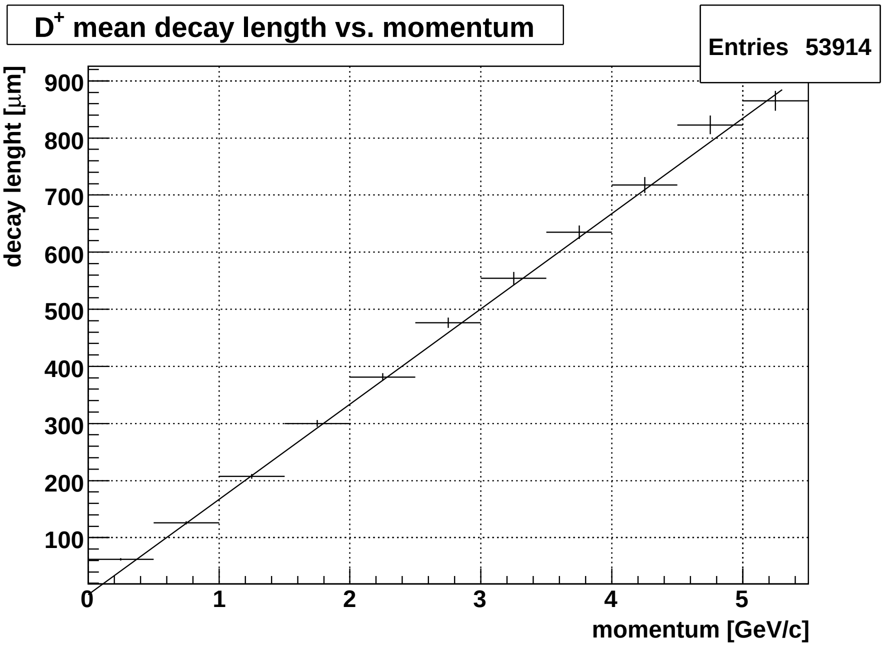

Figure 4.6: D^{+} decay length as a function of its momentum for Monte Carlo particles. (No cuts applied.)

These control plots show the character of the simulated data, impact of tracking on the data and mainly prove that the Monte Carlo simulated data as well as the reconstructed data are generated properly.

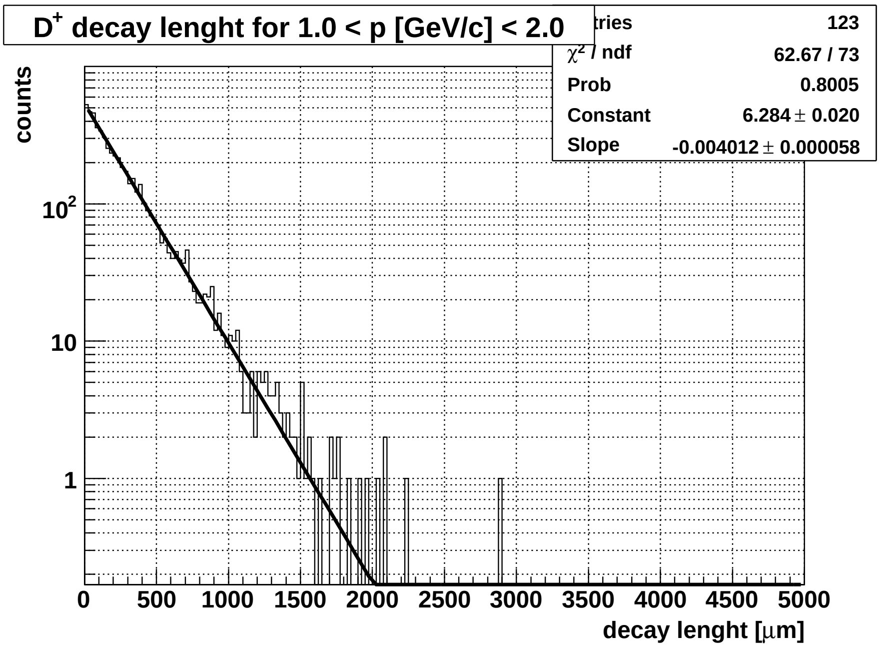

Figure 4.7: D^{+} decay length distribution fitted with exponential for Monte Carlo particles. (No cuts applied.)

4.3.1 Reconstruction efficiency

Plots Fig. 4.8 and Fig. 4.9 show π and K tracking efficiency as a function of p_T and efficiency of D^{+} reconstruction, respectively. In Fig. 4.8, the tracking efficiency for K is, compared to π, a little bit lower due to its shorter lifetime. For this probability calculation, we require correctly associated hits in both PXL layers and 15 hits in TPC.

For D^{+} (Fig. 4.9), the efficiency is calculated for three cases, i. e. after successful tracking of D^{+} daughters, after tracking with use of the gDCA cut (see Sec. 4.2) and after tracking with use of the gDCA cut with the best significance cuts for $1.0 < p_T < 1.5$ GeV/c (more in Sec. 4.4.2). The reconstruction efficiency for D^{+} is smaller than for D^{0} (see Fig. 3.1) because in D^{+} case one needs to reconstruct three daughter tracks with lower p_T than in two-body decay case. On the other hand, our determined efficiency for D^{+} is comparable to that of Λ_c (see Fig. 3.4) which undergoes three-body decay as well.

4.3.2 DCA resolution

Other important parameter of the detector is its pointing resolution of displaced vertex for different particles. Thereby we show DCA (to primary vertex) resolution in $x - y$ plane (Fig. 4.10) and in z-direction (Fig. 4.11) for π and K.

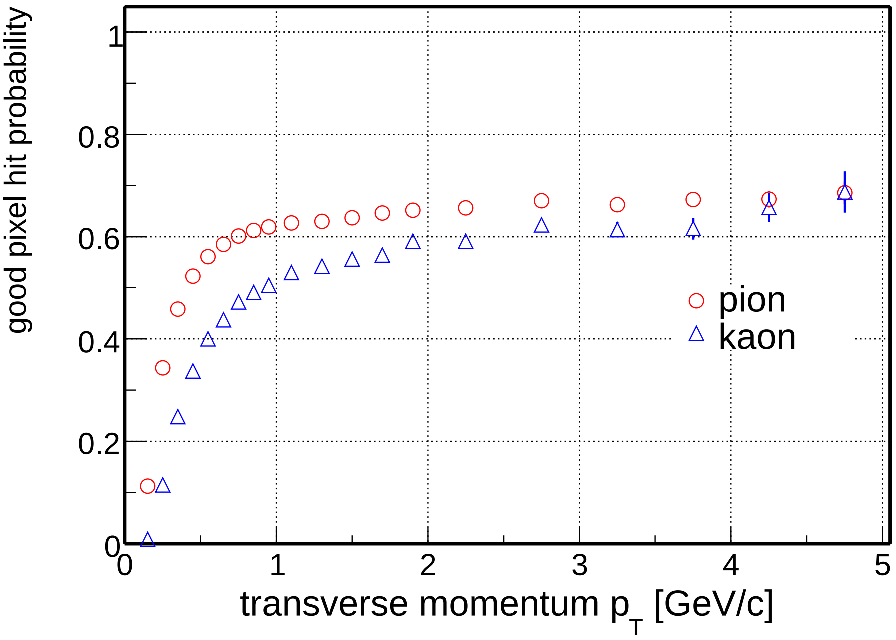

Figure 4.8: Reconstruction probability of pion and kaon tracks. (Requirements: $|\eta| < 1$, correctly associated hits in both PXL layers, 15 hits in TPC.)

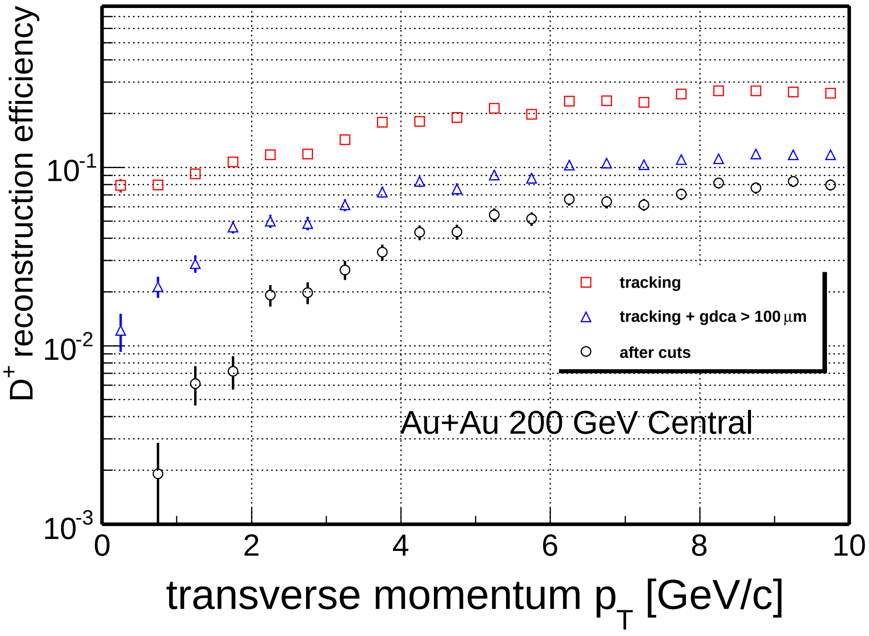

Figure 4.9: D^+ reconstruction efficiency after successful tracking of D^+ daughters and after applying cuts ($1819 < M_{inv} < 1919$ MeV/c^2, gDCA > 115 μm, $\cos\theta > 0.997$, $\mathrm{DCA}_{V0}/resol. < 2$. Requirement of good PID, that limits D^+ acceptance to $p_T < 4.8$ GeV/c, is not applied here (more in section 4.4.2).)

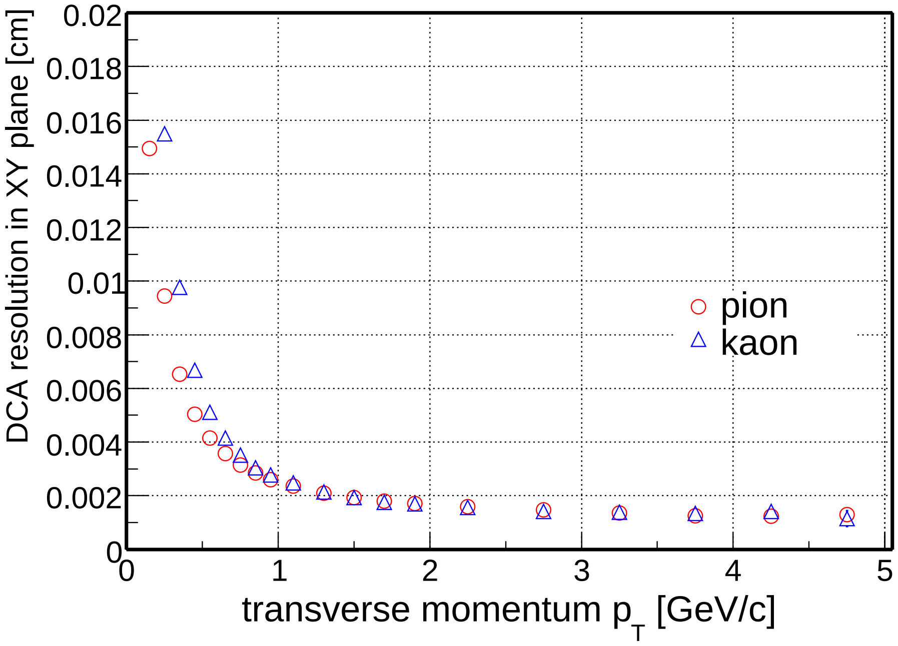

Figure 4.10: DCA resolution in $x - y$ plane for pion and kaon after tracking. (Requirements: $|\eta| < 1$, correctly associated hits in both PXL layers, 15 hits in TPC.)

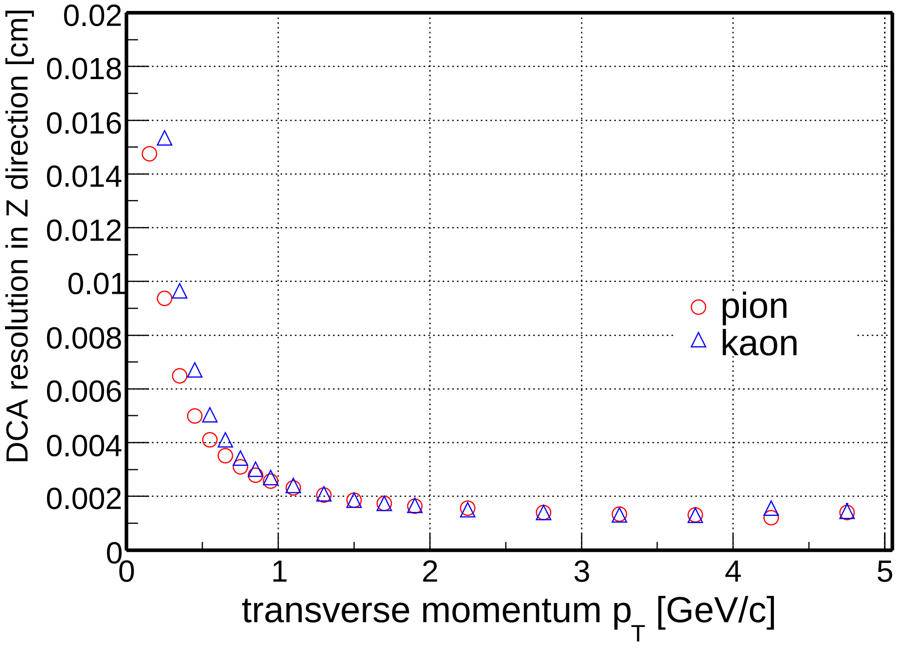

Figure 4.11: DCA resolution in z-direction for pion and kaon after tracking. (Requirements: $|\eta| < 1$, correctly associated hits in both PXL layers, 15 hits in TPC.)

4.4 D^+ signal significance

The aim of our analyses was to examine D^+ signal significance on conditions of new HFT design (upgr 15). We analysed significance up to D^+ $p_T = 2.0$ GeV/c, which is unique for STAR and HFT due to reasons mentioned in Sec. 2.2.2.

4.4.1 Rescaling of results to 100 M events

With STAR DAQ 1000 upgrade (commissioned in 2009), 100 million central $Au + Au$ events will be collected in less than 1 month of operation under realistic conditions (combination with other triggers, detector and RHIC duty factor). Therefore we estimate our significance for 100 M central events.

When we simulated 10 000 $Au + Au$ events, and wanted to get estimates for 100 M, the data had to be rescaled in a proper way. Furthermore because the number of D^+ produced per event in the simulation does not correspond real production, D^+ simulated signal has to be divided by following factor:

$$F = \frac{\langle \#\, D^+ \; per\ unit\ \eta \rangle}{\langle \#\, D^+ \; per\ unit\ y \rangle \langle B.R. \rangle} \tag{4.1}$$

In our case the number of D^+ per unit of η (pseudorapidity) is 2.5 (5 D^+'s in $|\eta| < 1$), number of D^+ per unit of y (rapidity) is an estimate for central $Au + Au$ collision equal to 0.8, branching ratio is 9.5%. These values give $F = 32.9$.

As mentioned in Sec. 4.3, p_T distribution of simulated D^+'s is flat. It has to be rescaled due to the fact, that the p_T spectra of real $Au + Au$ collisions is assumed to be governed by power-law:

$$\frac{1}{p_T}\frac{dN}{dp_T} = C \cdot \left(1 + \frac{p_T}{p_0}\right)^{-n}, \tag{4.2}$$

$$p_0 = \langle p_T \rangle \cdot \frac{n-3}{2}, \tag{4.3}$$

where C is a normalization constant, $\langle p_T \rangle = 1.0$ GeV/c and $n = 11$.

Beside these rescalings, the recomputation from pseudorapidity to rapidity has to be done.

4.4.2 Cut optimization

To separate signal from background, and therefore maximise the significance, we were tuning two earlier mentioned cuts (see Sec. 4.2). We were testing the amount of signal and background for various values of gDCA cut and cosθ cut. We obtained the best results when we increased the gDCA cut in discrete steps in range 100 - 235 μm, while doing the same with cosθ cut between 0.990 and 0.999. As a third cut was used narrower $K^-\pi^+\pi^+$ invariant mass M_{inv} window $1854 < M_{inv} < 1884$ MeV/c^2. For unambiguous particle identification (good PID) we assumed that π and K can be separated for $p_T < 1.6$ GeV/c, this is expected to be achieved with use of the MRPC TOF. For D^+ $p_T < 2$ GeV/c the use of the good PID requirement gives higher significance than if we take also misidentified $p_T > 1.6$ GeV/c particles. Therefore we used the good PID cut for all daughter particles in this calculation. All this was done separately for three p_T ranges: 0.5 - 1.0 GeV/c, 1.0 - 1.5 GeV/c and 1.5 - 2.0 GeV/c. We tried to obtain results for p_T in range 0.0 - 0.5 GeV/c too, but the signal was too small in this interval.

4.4.3 Results

Tuning of the cuts and the best significance cut are clearly shown in Fig. 4.12. Histograms in horizontal rows in the plot represent the amount of D^+ signal before rescaling, the amount of background before rescaling and computed D^+ signal significance after rescaling to 100 M events. It can be clearly seen for which cut significance is the highest in each p_T interval.

This "significance" is in fact true significance minus its error; we chose this quantity because it is more relevant than significance itself. If the significance error was of the same magnitude as significance, the significance itself would be meaningless. Hence significance minus its error brings correct information. We utilise this approach because of limited statistics of our simulation.

In the last three illustrative plots (Fig. 4.13, Fig. 4.14, Fig. 4.15), we show for mentioned p_T ranges, what would the D^+ peak with current significance look like. We repeat that these are results for 100 M central $Au + Au$ collisions at $\sqrt{s_{NN}} = 200$ GeV with the use of upgr15 of the Heavy Flavor Tracker detector for STAR.

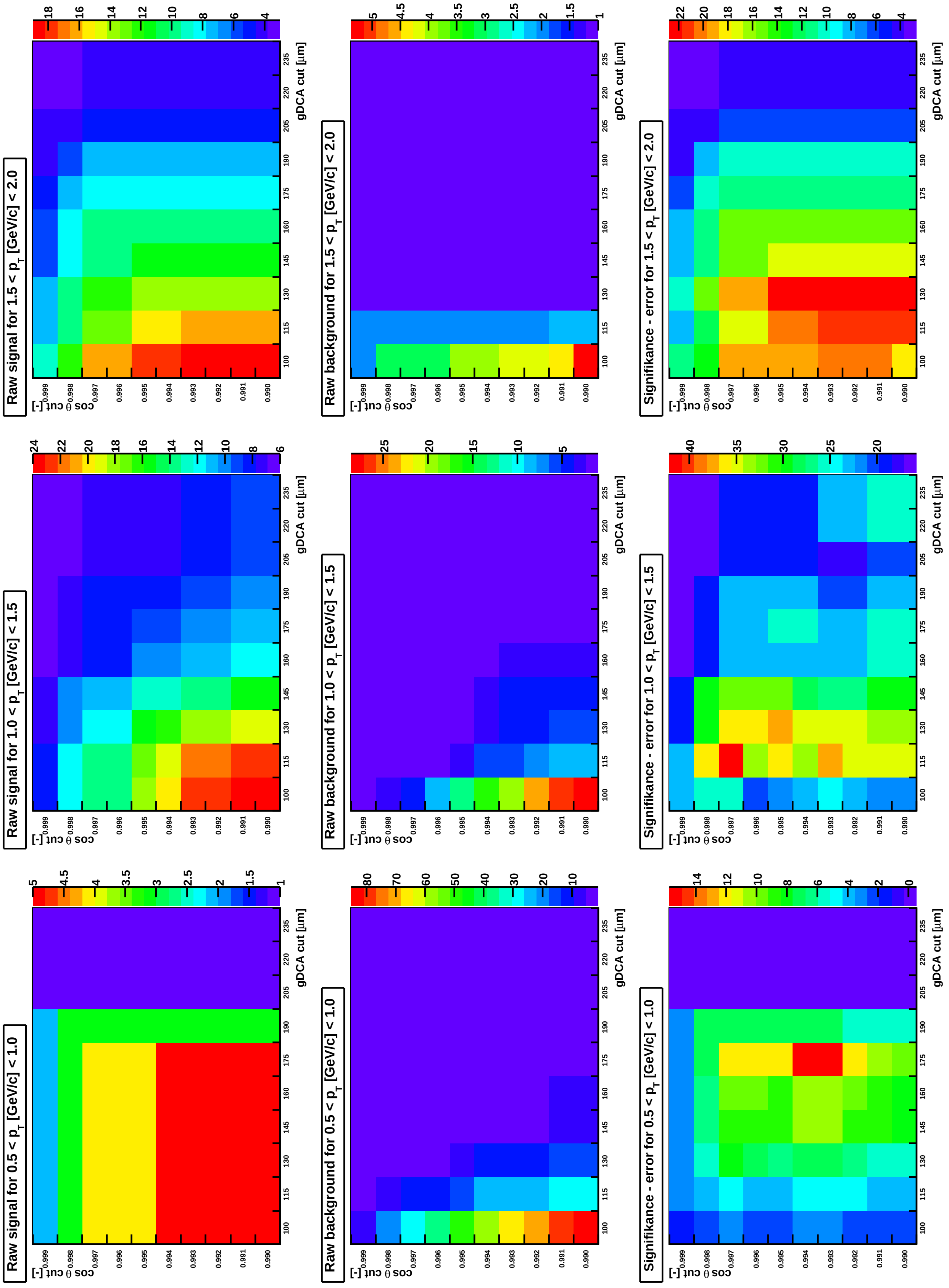

Figure 4.12: D^+ signal and background before rescaling and significance after rescaling to 100 M events as a function of gDCA and cosθ cut for three p_T ranges. ($1854 < M_{inv} < 1884$ MeV/c^2, good PID)

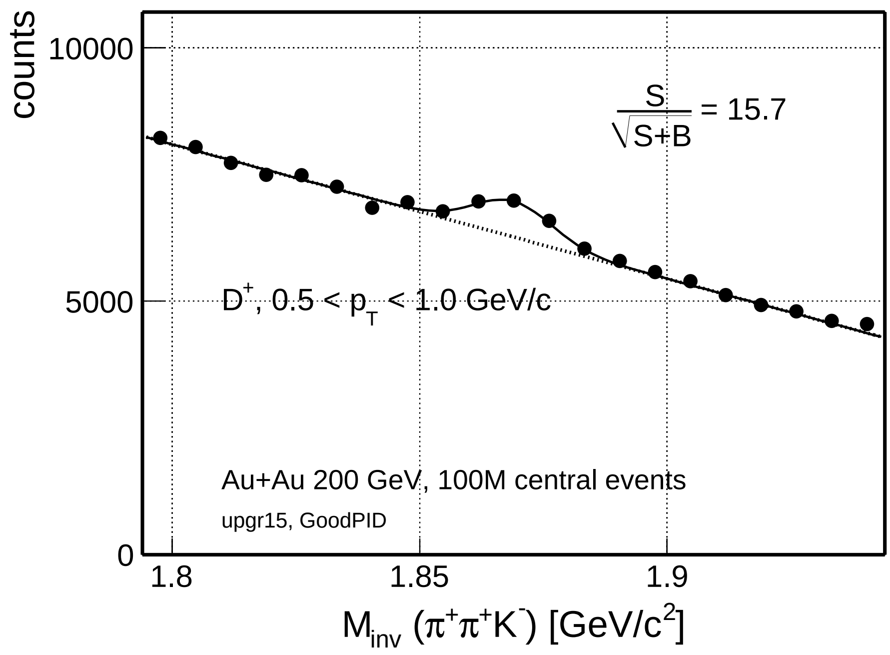

Figure 4.13: Expected D^+ signal for 100 M central $Au+Au$ collisions at $\sqrt{s_{NN}} = 200$ GeV, 0.5 < p_T < 1.0 GeV/c, upgr15. (good PID only)

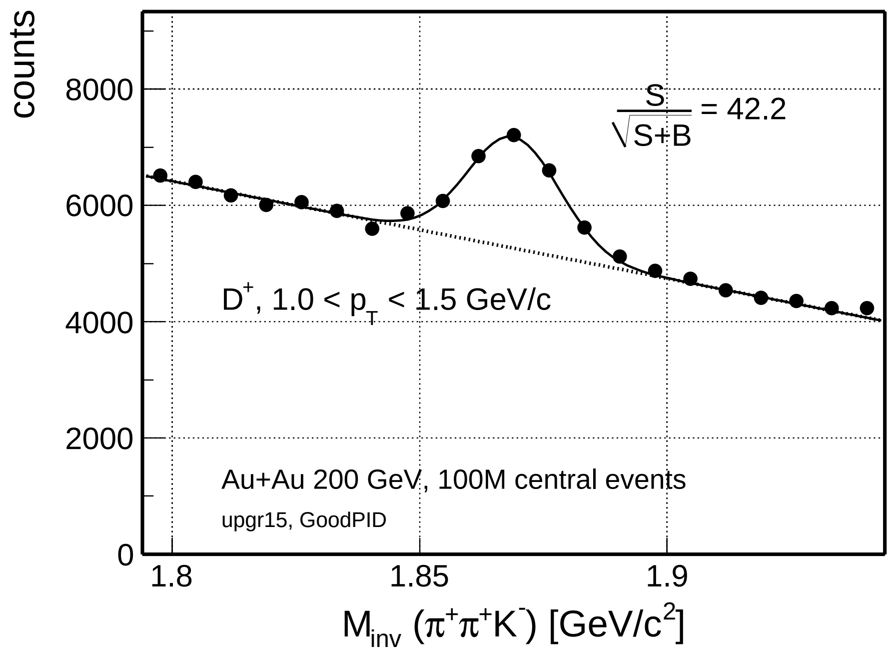

Figure 4.14: Expected D^+ signal for 100 M central $Au + Au$ collisions at $\sqrt{s_{NN}} = 200$ GeV, 1.0 < p_T < 1.5 GeV/c, upgr15. (good PID only)

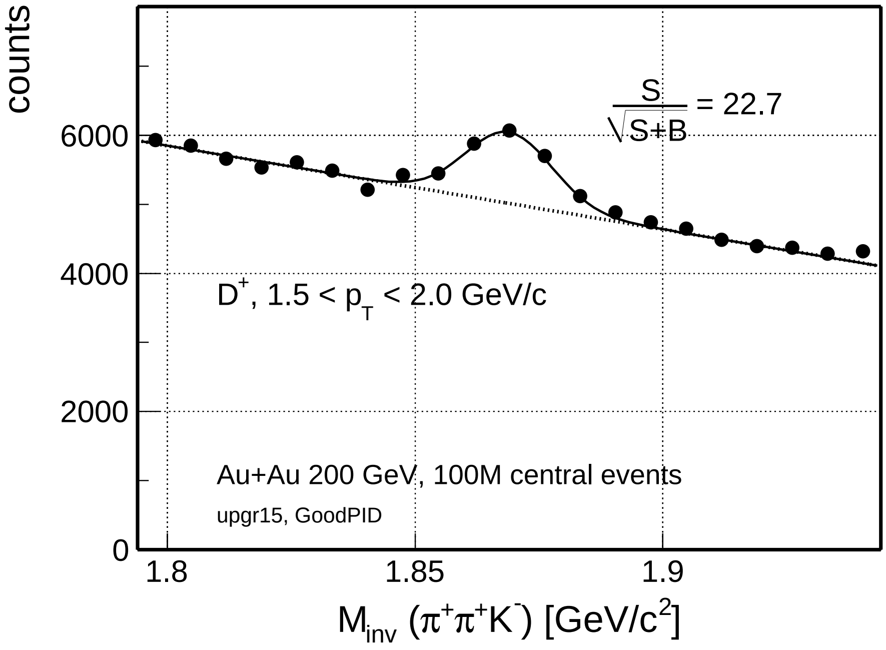

Figure 4.15: Expected D^+ signal for 100 M central $Au + Au$ collisions at $\sqrt{s_{NN}}$ = 200 GeV, 1.5 < p_T < 2.0 GeV/c, upgr15. (good PID only)

4.5 Conclusions

We have studied the performance of the new proposed detector Heavy Flavor Tracker for STAR in direct topological reconstruction of D^+ mesons via their hadronic decay channel for p_T up to 2.0 GeV/c. In the study of simulated data we have reached excellent significance of D^+ signal (see Tab. 4.2). This will further extend previously reported [48] capabilities of STAR with HFT upgrade to do precise measurements of partonic energy loss, charm collectivity and baryon/meson ratios. Systematic study of these quantities would help to understand processes which take place in hot and dense matter created in heavy ion collisions at RHIC.

p_T [GeV/c]	D^+ signal significance
0.5 - 1.0	15.7
1.0 - 1.5	42.2
1.5 - 2.0	22.7

Table 4.2: D^+ signal significance as a function of p_T.

These parameters of the detector can be achieved by using low mass monolithic active pixel sensors (PXL) for accurate spatial resolution and fast strip detector (IST) for high-level pointing resolution in the high multiplicity environment of heavy nuclei collisions with RHIC-II luminosity.

Chapter 5

Silicon Photomultiplier testing

As a part of the technical and practical subset of my master′s thesis, I participated in testing the Silicon Photomultiplier (SiPM) samples at Max Planck Institute for Physics in Munich. These photon-detecting devices are being developed to be used in high energy physics experiments, where they would replace recently used photomultiplier tubes (PMT). The advantage of SiPM compared to PMT lies mainly in their small size and low supply voltage. In this chapter we will shed light on the architecture and operation of the SiPM, introduce the high energy physics application and show results of testing these structures.

5.1 Silicon Photomultiplier

Silicon photomultiplier is a novel semiconductor device invented in the nineties; it was developed for photon detection. SiPMs have been continuously developed since then. Nowadays they are capable of detecting single photons [49]. Their dimensions are very small, the active area is usually of few mm^2, and most recently the detector casing exceeds size of the detector itself only slightly. Also they are quite fast, with pulses of few nanoseconds for a single photon event.

5.2 Layout and working principle

5.2.1 Avalanche photodiode

Avalanche photodiode (APD) is a semiconductor p-n junction (see Fig. 5.1) which is reverse biased with certain voltage slightly above breakdown. Under these conditions, any single free charge carrier (electron-hole pair) which appears in depleted region can initiate electrical breakdown. These charge carriers can be liberated by an impact of a photon. The hole and the electron are separated by applied electrical field and accelerated towards opposite electrodes. After short distance, the electron gains enough energy and creates new electron-hole pairs through impact ionisation of atoms. The same process undergoes every liberated electron. This is how the avalanche is created. After certain time the avalanche would engulf whole active volume of the detector and it would sustain itself for unlimited time period. This is why one has to decrease bias voltage below breakdown level, after breakdown of the diode occurs, to stop the avalanche. For this purpose, the diode is biased through an integrated quenching resistor in our case (see Fig. 5.3). If an APD fires, the resulting current causes a voltage drop on the diode and the avalanche is quenched [50]. Size of the resistor affects magnitude of the voltage drop and sets width of detected pulse. I fact the situation about quenching resistor is more complicated and has to be carefully considered in practice. During certain time after the breakdown, the APD has to recover, i.e. be brought back to the original value of the bias voltage. This time period is called recovery time. If a photon hits an APD in recovery stage, it will induce another breakdown, but the height of the output signal will be lower.

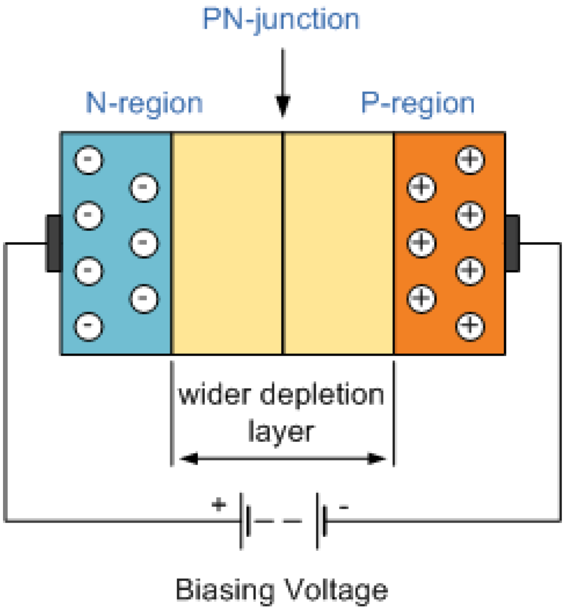

Figure 5.1: Reverse biased p-n junction.

Operation mode of a diode working above breakdown is called Geiger mode. In Geiger mode, when an avalanche is triggered, one obtains always the same output signal, independent of amount original free charge. This means that APD is a binary device which gives only information whether it fired or not.

5.2.2 SiPM

SiPM device is made of an array of avalanche photo diodes (APD) connected in parallel (see Fig. 5.2). As mentioned above, each cell now serves as a single photon detecting binary device. When a very weak photon source is used, the detector is capable of giving, thanks to parallel connection of APDs, information of how many photons hit the device at one moment. One firing cell (one APD) gives a signal of a certain amplitude; if there are more cells in the array firing at once, the resulting output signal will be an appropriate multiple of one cell amplitude. In a properly built device one single photon will start an avalanche, and therefore one can get information about number of detected photons (so called photon equivalents = p.e.). For such devices, if illuminated, one will get a signal amplitude spectra with several equidistant peaks for various photon equivalent numbers (e.g. see Fig. 5.16). In the many independent APDs also lies an advantage of such design. When one cell fires and is sensitive only in a limited way afterwards, all other cells can detect further photons meanwhile. Furthermore, probability of hitting the same cell twice in such a short time period, while using weak photon source, is rather low.

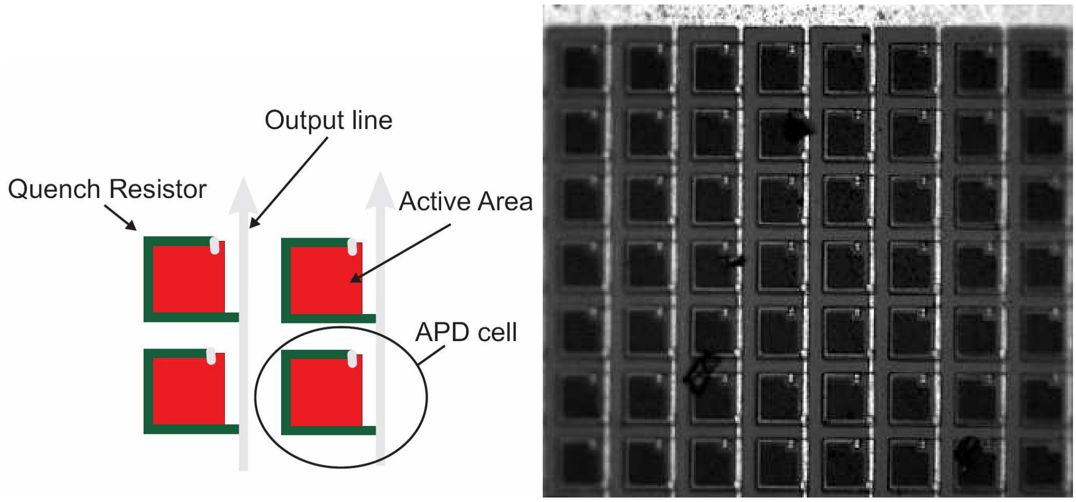

Figure 5.2: Schematic drawing and detailed photograph of a SiPM with polysilicon quenching resistor. Taken from [51, 52].

5.2.3 Quenching resistor

Polysilicon quench resitor

There are several ways how to implement the quenching resistor. The resistor can be made up of polysilicon structure deposited on the surface of silicon wafer (see Fig. 5.2). Drawback of this solution is that construction of the polysilicon resistor is very complex and expensive process. Furthermore, the resistor is also a light absorber and decreases sensitive area of the device. Such SiPMs are nowadays able to operate at room temperature and are planned to be used in future collider experiments (see section 5.3).

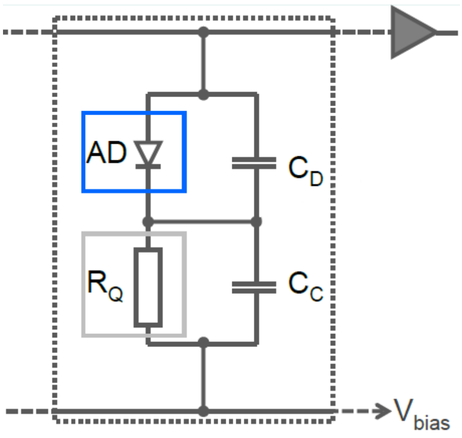

Figure 5.3: Electrical schematic representing one SiPM cell. *AD* is a photodiode, R_Q is a quenching resistor and C_D and C_C are their capacitances. Taken from [53].

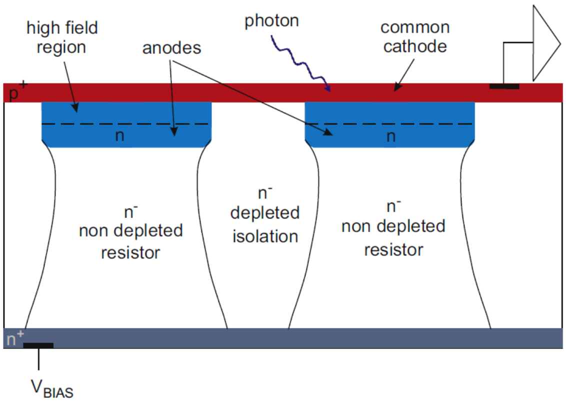

Figure 5.4: Schematic lateral cross section of SiPM wafer (2 pixels) with integrated quenching resistor. Taken from [54].

Bulk integrated quench resistor

Another recent approach is to use the silicon bulk as a quenching resistor. In Fig. 5.4 a schematic cross section of device with bulk integrated quench resistor is shown. Active area of the sensor lies in the high field region at junction of common p^+ cathode and n implantation at the top of the wafer. After applying bias voltage via the lower n^+ electrode, certain charge distribution arises along the device. The depleted region in between the pixels serves as a barrier which separates the pixels electrically. The non-depleted space in the silicon bulk behaves like a quenching resistor. Its size depends mainly on pixel pitch size, bulk doping level, wafer thickness, and the bias voltage. With increasing voltage is the non-depleted region getting thinner and thus resistivity raises. Because of quenching resistor size adjusting and need of depletion of whole thickness of the bulk, the silicon wafers have to be very thin (few tens of micrometers). Therefore, standard silicon wafers with thickness of few hundred micrometers have to be cut down (see Fig. 5.5). Thus, after implanting the bottom side of the silicon wafer it has to be fastened to another handle wafer, which serves as a mechanical support, and thinned up. Top side of the future device is implanted afterwards. This necessary step is a drawback because it makes the fabrication procedure more complicated. However, manufacturing these devices is simpler and cheaper than of sensors with polysilicon resistor. Another advantage of this technology is absence of polysilicon structure on the surface, and no metal contacts in the entrance window, and thus larger active area. One of the disadvantages of this approach is the rise of parasitic JFET in the sensor structure [54], which complicates the problem of quenching resistor. It cannot be treated as a simple resistor problem no longer, and the recovery time is 3-4 times longer than expected. The detector samples, we have studied, are using this concept of bulk integrated quenching resistor.

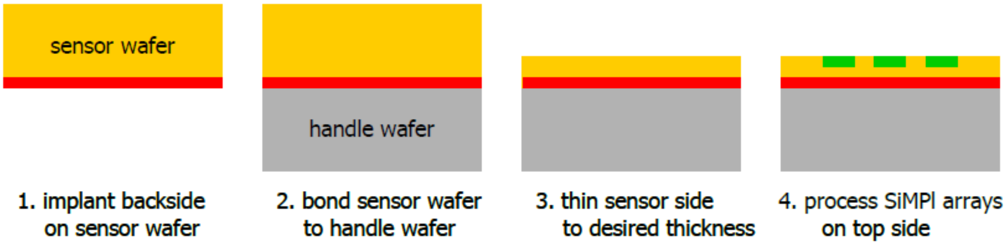

Figure 5.5: Sketch of wafer thinning process needed for fabrication SiPM with integrated quenching resistors. Taken from [53].

5.2.4 Some important SiPM characteristics

There are some more SiPM characteristic quantities which have to be explained for further discussion.

Dark counts

Due to thermal effects, electron-hole pairs are generated in the silicon bulk. When the device is operated above breakdown voltage, such liberated electrons can induce an avalanche and give so called thermal pulses. These pulses occur without illumination of the pixels. Hence, dark count rate is defined as a pulse rate in a perfect dark box. Dark counts depend on temperature, size of active volume, and breakdown efficiency (explained further). Dark rate also depends on the breakdown efficiency (explained further) because at higher breakdown efficiencies there is a higher probability that thermally generated electron triggers an avalanche.

Gain

Gain G is a factor which gives us an information about total number of charge carriers in the avalanche obtained in one event ($\sim 10^6$). This determines magnitude of total avalanche charge Q_{av} as well. Value of Q_{av} is fixed; irrespectively to the initial free charge amount in active volume of the device.

$$Q_{av} = G \cdot e = C_{pix}(U_{bias} - U_{break}) = C_{pix} \cdot U_{over} \tag{5.1}$$

where e is the elementary electrical charge, C_{pix} is pixel capacitance, U_{bias} and U_{break} are bias and breakdown voltages, respectively. U_{over} is called overbias voltage. From (5.1) it is obvious that the gain is directly proportional to the overbias voltage and independent of number of electron-hole pairs created by incident particle. For best SiPM operation is important to choose proper overbias (usually 10% of the breakdown voltage) because of reaching highest possible breakdown efficiency (close to 100%). However, some unwelcome effect with increasing overbias can occur, e.g. enhanced dark rate.

Photon detection efficiency

Photon detection efficiency (PDE) η_{PDE} is a probability that an incident photon induces an avalanche. It is given by a product of quantum efficiency η_Q, breakdown efficiency η_B and geometrical factor η_G:

$$\eta_{PDE} = \eta_Q \cdot \eta_B \cdot \eta_G \tag{5.2}$$

Quantum efficiency is probability that the photon creates electron-hole pair in high field region; breakdown efficiency is probability that an avalanche is generated by an electron-hole pair created in the active region. The breakdown efficiency is enhanced with increasing overbias voltage. Geometrical factor is a fraction of active to whole area of one pixel.

Optical crosstalk

As an avalanche is evolving in high field region of an APD, some of charge carriers can recombine and emit a photon thereby. This photon can travel through the silicon wafer and if absorbed in active region of a neighboring pixel, it could initiate an avalanche. From the breakdown of the neighboring pixel one gets a fake pulse. When measuring dark signal distribution, optical crosstalk can be calculated form ratio of areas of 1 and 2 p.e. peaks. This method is enabled by the fact that almost only single cells do fire when the device is unlit; hence the signal coming from two fired cells is given almost entirely by the optical crosstalk. This unwelcome effect can be overcome by adding trenches in between the pixels [55].

Afterpulsing

This effect, causing fake signals as well, arises due to existence of additional levels in a band gap region of semiconductor energy level structure [37]. Charge carriers can be trapped in these metastable levels for a time and released afterwards with some delay. This freed again particle can trigger another avalanche and therefore give a fake pulse coming after the real one. This is where the term afterpulsing comes from; the effect of afterpulsing becomes significant when the device is operated at low temperatures because the lower the temperature is, the longer stays the charge carrier trapped.

5.3 Physics applications of SiPMs

As mentioned in beginning, the advantages of silicon photomultipliers are their small size, capability of single photon detection, and low supply voltage. Experiment CALICE which will be placed at proposed International Linear Collider (ILC) intends to use SiPM instead of classical photomultiplier tubes (PMT). In the HCAL detector (hadron calorimeter), light from scintillator tiles (see Fig. 5.7) will be detected with SiPMs using polysilicon quench resistor [56]. This solution will make it possible to reach high granularity of the detector, which is needed for high jet energy resolution.

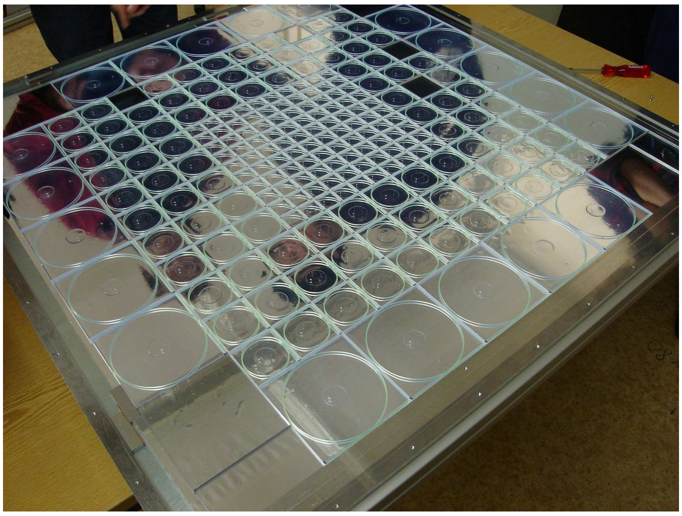

Figure 5.6: Scintillator tiles assembled to one complete active layer of HCAL detector. Taken from [56].

Second experiment which plans to use SiPMs is the MAGIC. The MAGIC (Major Atmospheric Gamma-ray Imaging Čerenkov telescope), as in from its name obvious, is designated to detect very high energy cosmic gamma-rays [51]. These γ-rays induce in the atmosphere particle showers. The secondary particles generate in the air Čerenkov radiation which can be detected in focal point of huge parabolic mirror (see Fig. 5.6). The usage of SiPMs will lower γ-ray detection threshold to 10 GeV and improve sensitivity of the whole device. Another future astrophysics experiment which intends to utilize these new detectors is the Cherenkov Telescope Array (CTA) project.

5.4 Testing of SiPM samples

Our objective was to measure various characteristic quantities of second development series of silicon photomultipliers fabricated at Max Planck Institute for Physics in Munich. These devices are using the concept of the bulk integrated quenching resistor (see section 5.2.3). Pixels of the tested detectors are of hexagonal shape and are assembled into three different arrays (see Fig. 5.8). The "flower" is made of 7 pixels; "double flower" contains 19 pixels and the largest structure is an array of 10×10 pixels. A separate single pixel is also included on the this device. Produced samples differ slightly in pixel pitch (~ 130 μm)

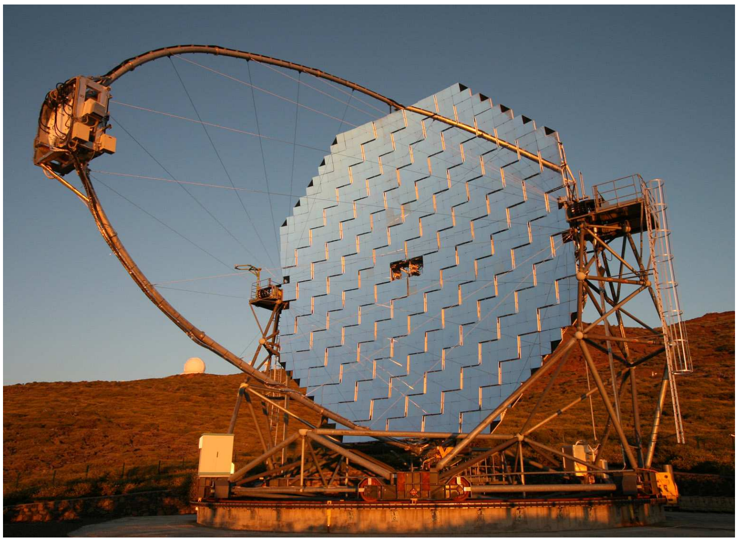

Figure 5.7: MAGIC telescope device.

and gap of insensitive area between pixels (~ 15 μm). Measurements of the same characteristics within various structures with different pitch and gap will give worthy information as breakdown voltage, quenching resistor size, recovery time, geometry dependence, etc. These data are important especially for sensor developers to fine-tune their simulations, and to carry out further iterations. It also shows whether this concept may be able to serve as a single photon detector in general.

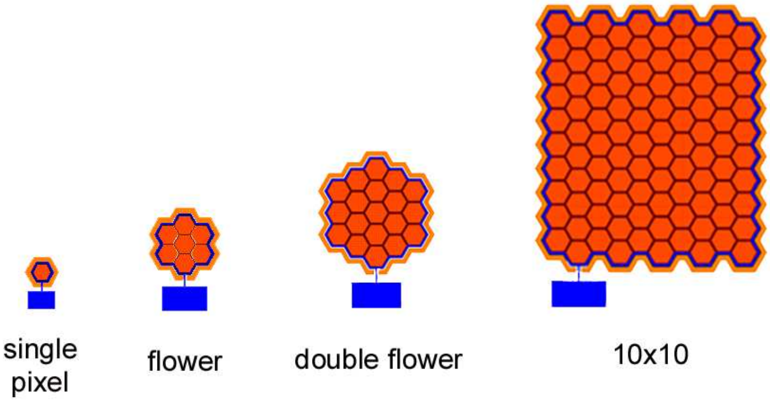

Figure 5.8: Shapes of pixel structures used in SiPMs fabricated at MPI in Munich. Taken from [52].

5.4.1 Check measurements

Before we started desired measurements which will give us required information about tested device performance, we conducted some basic tests to be sure that the device is working properly.

The very first thing is observation of output signal shape of unlit sensor. Fig. 5.9 (top) shows clear signal of one fired cell (one APD). It is important to see solid, not too much changing, baseline and not too many pulses occurred before the cell is fully recovered (brought back to the bias voltage level) (see Fig. 5.9 bottom). The unstable baseline can be a signature of excessive influence of high dark counts, afterpulsing or both (see sec. 5.2.4). This effect disables us to set suitable trigger levels for further measurements and makes the measurements infeasible. Firing of non-recovered cells causes distortion of signal amplitudes and hence confusion of amplitude spectra. It can result in higher pedestal or also in amplitude spectra smearing. One can significantly reduce these unwelcome effects by cooling the sensor down.

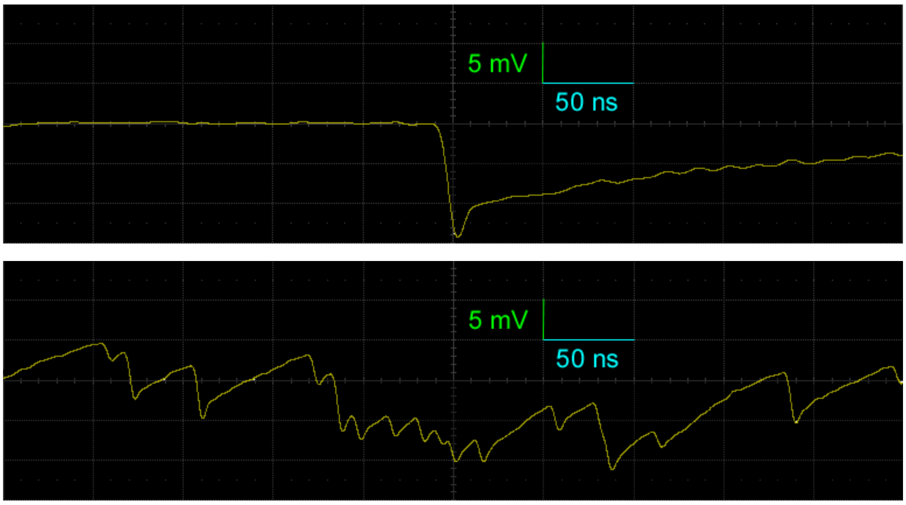

Figure 5.9: Example of observed output signals of tested SiPMs. **Top:** clean signal of one fired cell, stable baseline. **Bottom:** Very noisy signal with non-recovered cells firing, unstable baseline, unsuitable for any measurement.

The first measurement is shown in Fig. 5.10. It is a relation between the single cell signal amplitude (or 1 p.e., see section 5.2.4) and the overbias voltage fit with a linear function. One can clearly see that the experimental data is in good agreement with the linear fit and therefore with equation 5.1. This is because the amplitude is directly proportional to total avalanche charge. Hence in this point of view we can say that the device is working standardly concerning this voltage range.

Breakdown voltage as a function of temperature you can see in Fig. 5.11. In such temperature range the breakdown voltage should behave linearly [57]. From the plot it is obvious that the dependence is approximately, but not perfectly, linear. However, this result is good enough for us especially because this measurement was done at device originating from the first development series. These sensors have worse characteristics than the second series devices which we intend to probe. Behavior of temperature dependence of breakdown voltage

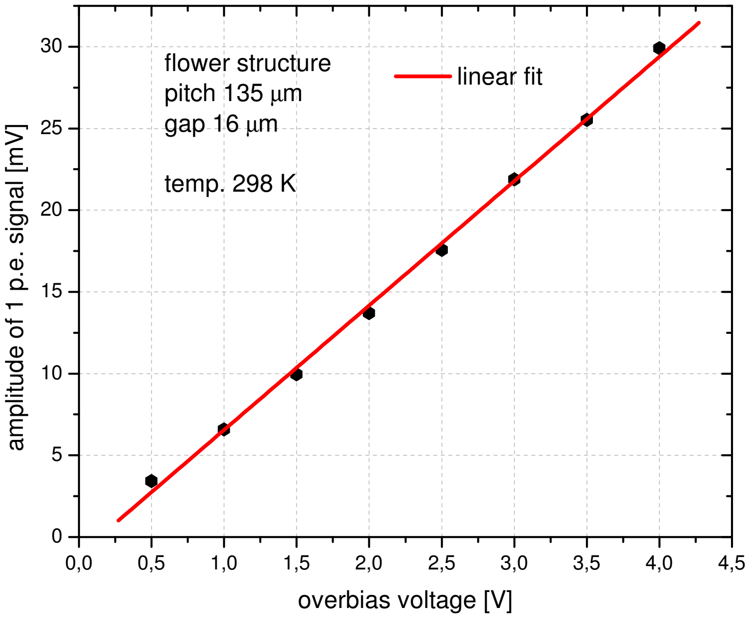

Figure 5.10: Amplitude of 1 p.e. as a function of overbias voltage. Fit with a linear function.

is especially of interest when one wants to carry out measurements at various temperatures for comparison; overbias has to be adjusted properly to set the same matching detection conditions according to the temperature dependence. The reason why we do cool down is that there are some technological problems at the moment which cause too high dark rate. Cooling the sensor down is a way how to lower dark counts.

The last check measurement, dependence of dark count on overbias voltage, is shown in Fig. 5.12. To explain this picture, one has to take into account more effects. With increasing overbias, breakdown efficiency is enhanced as well and more thermal electrons can start an avalanche. On the other hand, size of quenching resistor is with rising overbias increasing (as mentioned in Sec. 5.2.3) and avalanche current is growing up. At some point the quenching resistor size is not high enough to stop the avalanche and quenching condition is broken (for more detail see [50]). All this means that until quenching condition is fulfilled, dark rate raises linearly due to higher breakdown efficiency. After violation of quenching, dark rate will start to increase much more steeply because of rise of self sustaining avalanches. In our plot one can observe described behavior with the mentioned turning point at about 3.9 V overbias. Best operational overbias voltage for such devices is slightly below the turning point because of the highest breakdown efficiency. In general it is said that the most suitable overbias is of 10% above breakdown voltage. When breakdown voltage of our tested sensors

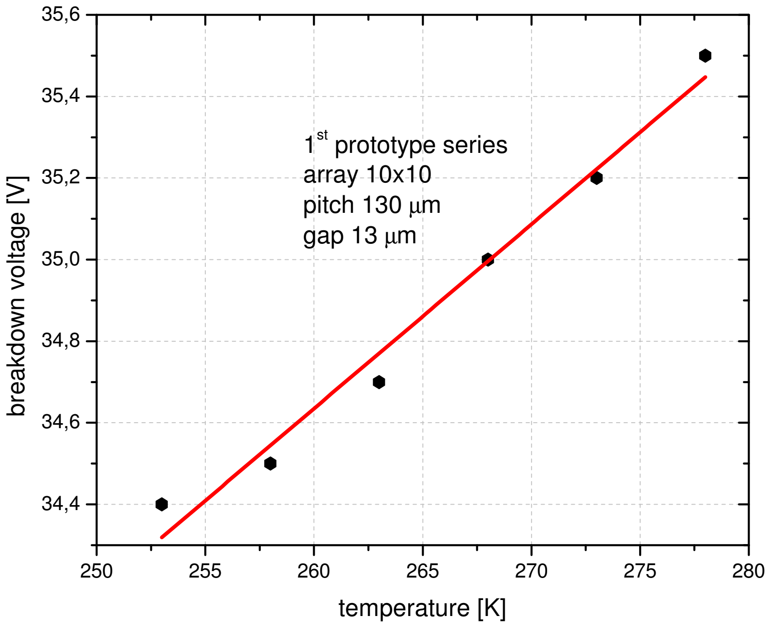

Figure 5.11: Breakdown voltage as a function of temperature. Fit with a linear function.

is about 35 V, our results are corresponding to this statement. However, there are more unwanted effects which can forbid measurements with optimal breakdown efficiency, e.g. changing signal baseline or unacceptable rate of dark counts. This is why we had to perform this measurement at 233 K. At higher temperatures the baseline was too unstable to get meaningful data.

5.4.2 Response to 800 nm laser illumination

The main goal of our work with SiPMs was to survey response of second development series devices to laser beam. The devices are designed to detect light with maximal PDE at wavelength of 400 nm. Unfortunately, only 800 nm laser beam was available at the test site. With use of this wavelength there is a disadvantage of lower quantum efficiency, but also this laser provides desired information.

We had a set of six samples from second generation of SiPMs fabricated at MPI. For our measurements we chose the one with the lowest level of leakage current (pixel pitch 135 µm, gap 15 µm). Further, on this device we chose double flower structure sensor with 19 pixels (see Fig. 5.8). Then we did several measurements with various values of temperature, overbias voltage and laser intensity. Because we were not able to get an accurate value of laser output intensity, in further descriptions we will only use terms “low”, “medium” and “high”. Laser pulses were of 3 ns width and frequency of 10 kHz.

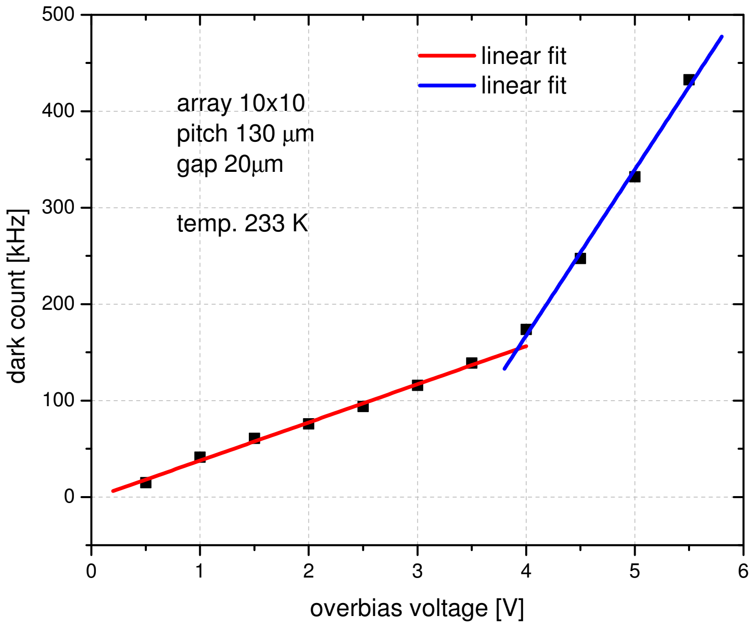

Figure 5.12: Dark count as a function of overbias voltage. Fit with a two different linear functions. The point, where the quenching condition starts to be not valid can be seen at the point of crossing of the two linear fits (at 3.9 V).

We tried to find values of those three quantities for which we get the clearest amplitude spectra of output signal from the device. That means, we wanted to see as many and as sharpest photon equivalent peaks as possible. It appeared that we obtain the best results at 1.0 V overbias voltage; this is why we will show you only measurement results at this voltage value.

In Fig. 5.13, normalised pulse height distribution of mentioned double flower device at medium laser level and various temperatures is displayed. It can be clearly seen that with decreasing temperature, height of the peaks above background is significantly enhanced. For lower temperatures we can also distinguish more peaks at higher photon numbers. Next effect is suppression of 1 p.e. peak. The 1 p.e. peak is for higher temperatures enhanced especially because of dark pulses. However, dark count decreases with temperature exponentially and 1 p.e. peak decreases as well. Lower dark count could also be a reason why relative peak height changes. At higher dark counts there are more not fully recovered cells. If these cells give a signal, it will be more or less lower. This effect causes broadening of the peaks and hence their larger overlap which makes the peaks relatively lower. There are two more effects in the plot which have to be further investigated. The first of them is the smaller height of higher photon equivalent peaks at lower temperatures. An explanations of this effect could be a saturation caused by intensive laser output. The second one is much lower 1 p.e. signal amplitude (and hence distance between single peaks) at room temperature (300 K), which could be caused by inaccuracy of breakdown voltage determination. We think that these two effects are also strongly affected by the dark count, but detailed mechanism is not completely clear at the moment.

Next plot, Fig. 5.14, shows detector response to different laser intensity levels for fixed temperature of 273 K. As expected, with raising laser level, the whole distribution is shifted to higher photon numbers. Also, at higher laser levels the peaks are getting broader and the distribution is not so smooth. This broadening has very similar reason to the broadening caused by dark count mentioned in the previous paragraph. In this case the dark count is "replaced" by high photon impact rate and hence there are more non-recovered cells (saturation). For low laser level, one can see at the beginning of the distribution one more small peak. This peak represents noise of the device itself and of the readout electronics. The noise peak can be seen especially at low photon rates because in this situation there is lower signal to noise ratio.

Now, we focus on one amplitude spectra. We can fit it with a sum of multiple Gaussians. In Fig. 5.15 one can see that background is caused only by overlap of neighboring Gaussians and hence there are no additional sources of background signals. The next important thing is that the peaks are actually equidistant and we can be sure that they really represent current number of firing cells. In Fig. 5.15 amplitude spectra is shown at 300 K, 1 V overbias and medium laser; distance of neighboring peaks is 4.5 ± 0.4 mV. This in agreement with signal height measurements of dark signal. Especially this plot is very valuable because it shows capability of this device to serve as a single photon detector at room temperature.

Figure 5.16 is of the same fashion as the previous one with the change that the data were taken at temperature of 253 K. As mentioned earlier, relatively higher and more peaks can be seen at this low temperature. Both of these effects occur due to smaller FWHM[1] of the peaks. This plot shows the best results obtained during our measurements. The peaks are high above background, the distribution is pretty smooth, and peaks up to 9 p.e. can be distinguished.

We also started the same measurements with 10×10 structures, but at time of writing this text the measurements were not optimized to get valuable information. Unfortunately, these measurements were very badly influenced by used laser device itself. When switched on, it caused large growth of noise in the signal even if the light output was disconnected and hence the SiPM device was not illuminated. Obviously, this effect is much more significant for arrays with larger number of pixels. For this reason some changes in experimental setup have to be done and the measurements repeated. Other reason for the bad signal could be that breakdown takes place only at the edge of the pixels.

---

[1] FWHM - Full Width at Half Maximum

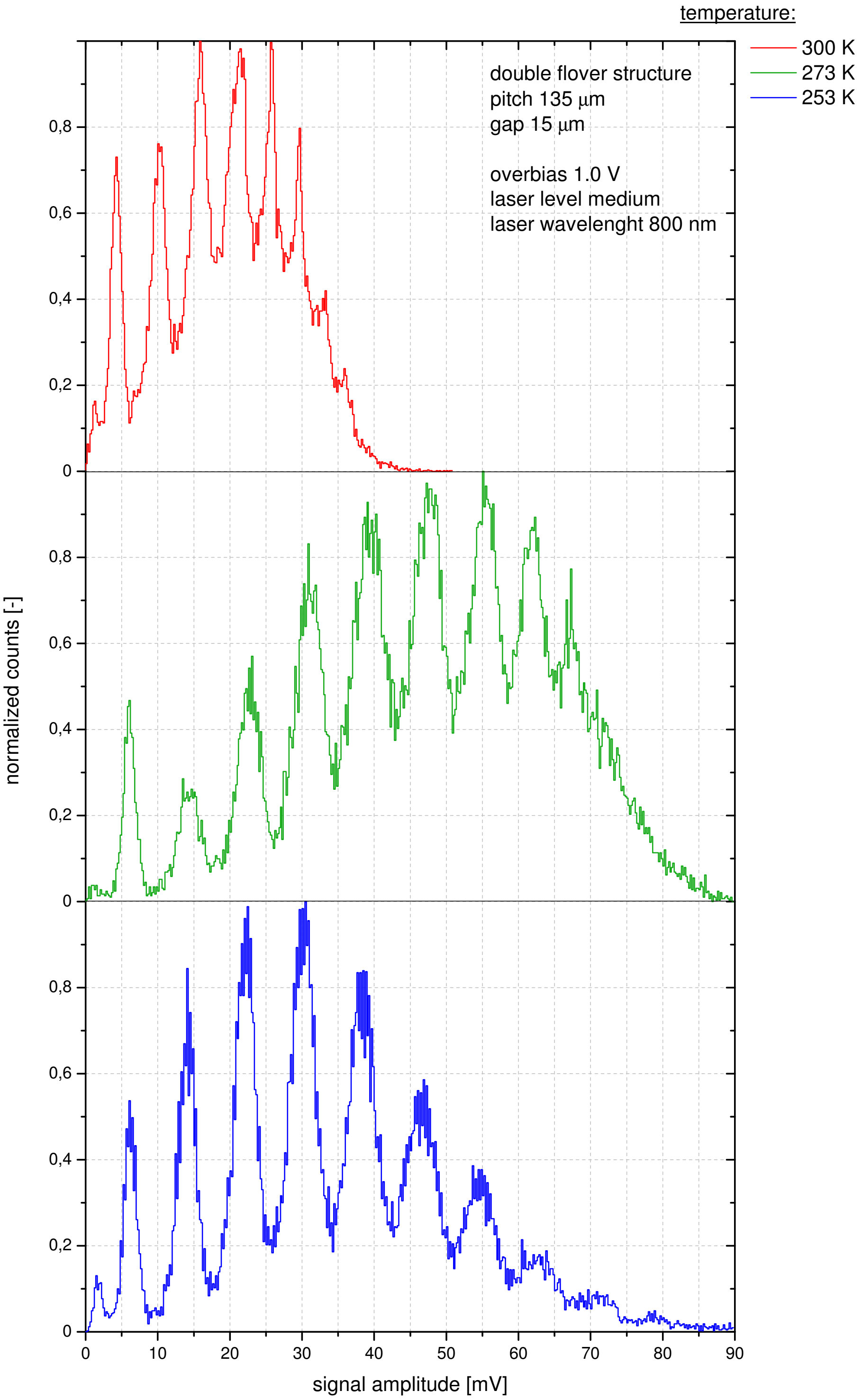

Figure 5.13: Amplitude spectra of output signal at medium laser level and 1 V overbias for various temperatures. The highest count number is normalized to unity for each temperature.

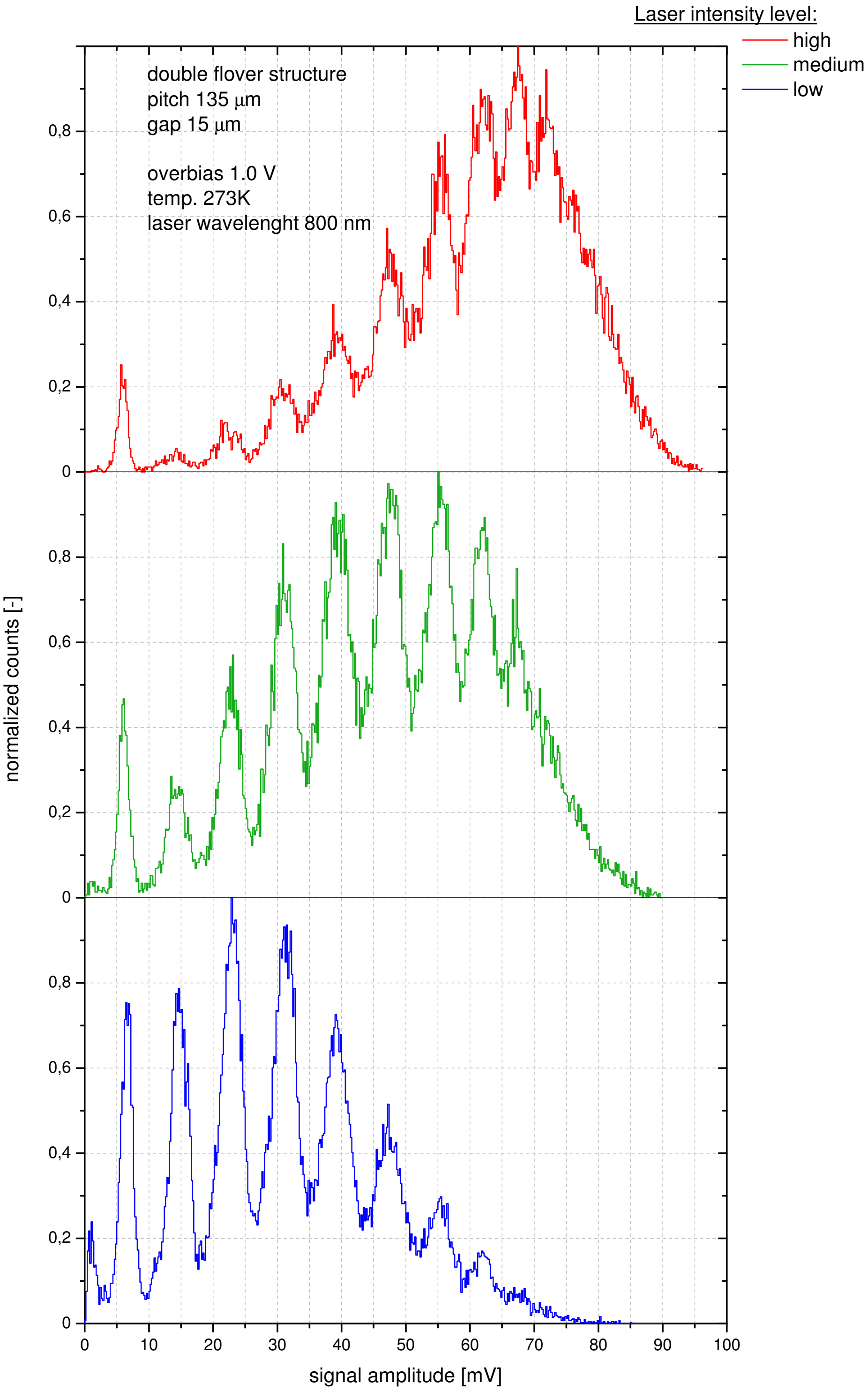

Figure 5.14: Amplitude spectra of output signal at temperature of 273 K and 1 V overbias for various laser levels. The highest count number is normalized to unity for each laser level.

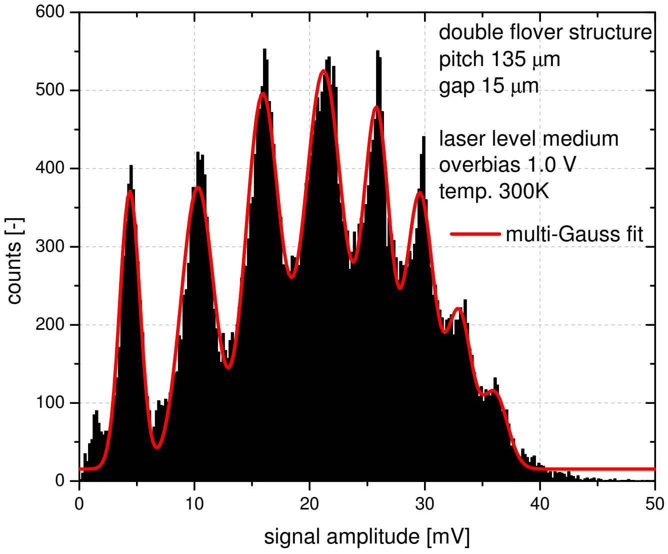

Figure 5.15: Amplitude spectra of output signal at temperature of 300 K, 1 V overbias and medium laser level fit with a sum of eight Gaussians. Distance of neighboring peaks is 4.5 ± 0.4 mV.

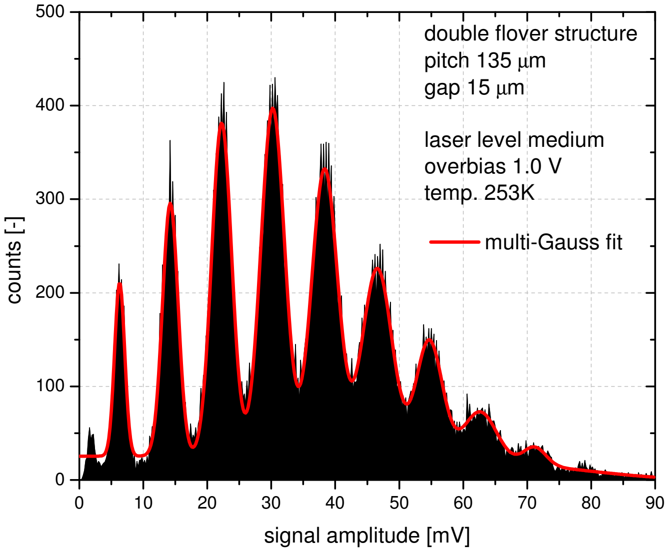

Figure 5.16: Amplitude spectra of output signal at temperature of 253 K, 1 V overbias and medium laser level fit with a sum of nine Gaussians. Distance of neighboring peaks is 7.5 ± 0.5 mV.

5.5 Conclusions

We investigated silicon photomultipliers with bulk integrated resistors of the second development generation constructed at Max Planck Institute for Physics in Munich. We tested their features and response to laser light. From available detector structures with different numbers of pixels we chose so called "double flower", composed of 19 pixels. The measurements results show that the sensor responses to various laser levels at different temperatures in most cases as expected and could be capable of detection single photons even at room temperature. To be absolutely sure of the single photon detection ability, further measurements with single photon source should be done.

Our tested detectors intend to be improved to serve as single photon devices with large pixel arrays. After reaching this technical level they are planned to be used in future physics experiments where detection of very low light amounts are desired. These are e.g. CALICE experiment at ILC which plans to use SiPM for readout of scintillation detectors or future astrophysics experiments like MAGIC which intend to detect Čerenkov light created in the atmosphere with SiPMs.

Summary

During work on this diploma thesis we analysed simulations of the Heavy Flavor Tracker, a new proposed vertex detector for the STAR experiment at RHIC. We maximised significance of D^+ meson signal at low transverse momentum. We reached quite encouraging results (see Sec. 4.5) which showed that STAR with the HFT upgrade would be capable to reconstruct D^+ mesons directly via their hadronic decay channel $D^+ \rightarrow K^-\pi^+\pi^+$. This would enrich STAR physics programme which intends to study properties of hot and dense nuclear matter created in ultrarelativistic ($\sqrt{s_{NN}} = 200\,\mathrm{GeV}$) heavy ion collisions at RHIC. Heavy flavor hadrons, products of heavy quarks fragmentation, such as $B^\pm, D^0, D_s^\pm, D^\pm, \Lambda_c$ or J/ψ, are believed to serve as good probes to the medium. Space-time evolution, thermalisation, and other properties of this matter are going to be studied through observables like flow, nuclear modification factor, total charm and beauty production cross section, etc. In the field of HFT simulation, there is a wide range of further possible work, e.g. on performance studies for other particles and quantities.

The second objective of silicon photomultipliers (SiPM) testing has also been accomplished. We studied performance and properties of second production series of SiPM with bulk integrated quenching resistor constructed at Max Planck Institute for Physics in Munich. We discovered that they could be capable of detecting single photons even at room temperature within small pixel arrays (19 pixels) (see Fig. 5.15). These devices are still in development They have to be further tested and more deeply understood. Hence, there are several parameters to be measured in the future. Information obtained within our work with SiPMs would serve as a feedback to SiPM developers and also could help to fine-tune detector simulations. However, a lot of work on SiPM design has to be done to reach desired parameters, until it can be used in planned future accelerator and astrophysics experiments.

Acknowledgment

I am very grateful Mgr. Jan Kapitán for invaluable help and guidance during my work on HFT simulations. Further, I would like to thank dipl.phys. Christian Jendrysik for introduction to the issue of silicon photomultipliers and related measurements. I am also very thankful to my supervisor Mgr. Jaroslav Bielčík, PhD. for his worth hints which helped to improve the diploma thesis. I wish especially to thank Michaela Klepáčková for priceless language corrections.

Appendix A

APS testing setup

As a part of this thesis, is was planned to make an upgrade of existing setup for active pixel sensors (APS) readout in the Nuclear Physics Institute in Řež near Prague of the Academy of Sciences of the Czech Republic (NPI of ASCR). The purpose of the new setup is to probe parameters and properties of APS like spatial and energetic resolution, and particle detection efficiency.

The original setup consisted of a motherboard, where data acquisition (DAQ) was placed and a mezzanine board carrying the sensor itself. The output data are sent out via SCSI[1] bus with pseudo-SCSI transfer protocol. Readout was provided by personal computer (PC) via quick USB[2]; therefore, a SCSI-to-USB converter was placed between PC and the motherboard. The whole device was driven by Xilinx Spartan 3 [58] FPGA[3]. We decided to replace the old APS by a commercial APS Cypress IBIS4-1300 [59]. Because of the new APS chip, we also had to project a new mezzanine board for this sensor. Such change in design requires new software for device operation as well as for readout in the PC. A block scheme of the APS readout setup is shown in Fig. A.1.

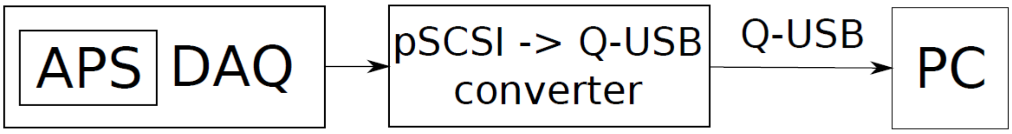

Figure A.1: Block scheme of readout chain for the APS.

Readout software

A preliminary version of the software for readout and data visualisation in the PC was created in Lab Windows CVI environment. It is designed to process digital

---

[1] SCSI - Small Computer System Interface

[2] USB - Universal Serial Bus

[3] FPGA - Field-Programmable Gate Array

data in the form in which they leave the APS chip. The primary purpose of the programme is to display the pattern obtained from the APS. A screenshot of this software is shown in Fig. A.2. On vertical and horizontal axis, a number of the pixel in x and y is shown. The color represents the amount of integrated charge in current pixel. For this current plot, artificially generated data were used, and hence there is no connection to real picture from the sensor. For tuning purposes, capability of visualising individual quadrants of the whole array, and readout of arrays of arbitrary dimension was also implemented in the programme. This software was successfully tested on a set of binary files of the same form as the expected APS signal.

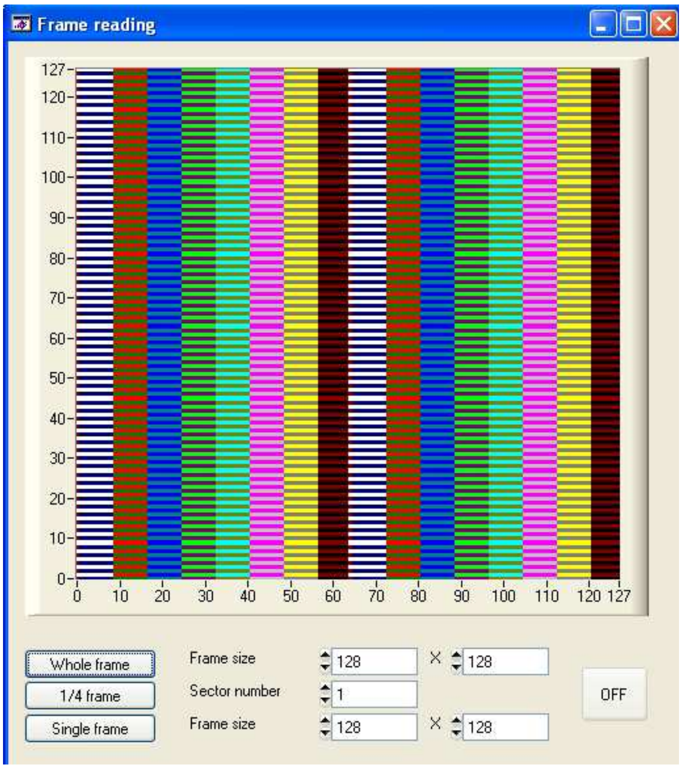

Frame size 128 × 128
Sector number 1
Frame size 128 × 128

Figure A.2: Screenshot of the readout and data-visualising software testing.

Device operation

As mentioned above, for a new APS chip, new control software had to be written for the FPGA. For FPGA programming we used VHDL[4]. We utilised the old module for communication with the paralel output interface, but the remaining modules had to be designed in a completely new way, due to the new sensor. Block scheme of inner architecture of the FPGA and the APS and communication

---

[4] VHDL - VHSIC Hardware Description Language, VHSIC - Very-High-Speed Integrated Circuit

between them can be seen in Fig. A.3. The master logic which controls the sub-modules, and hence operation of the whole device, is placed the module "FPGA APS interface". The "Reset" module drives the APS reset shift register which brings individual pixel to their initial state. Reset pattern has to be in correlation with the sampling ("Sample" module) sequence sent to "Master logic" which is dealing with selection of pixels to be read out. The correlation between these two signals is of great importance because it determines integration time of the sensor. The third sub-module called "Readout" (also denoted RDO) communicates with ADC[5] on the sensor and receives output data flow. The APS "Sensor core" represents the detection element itself.

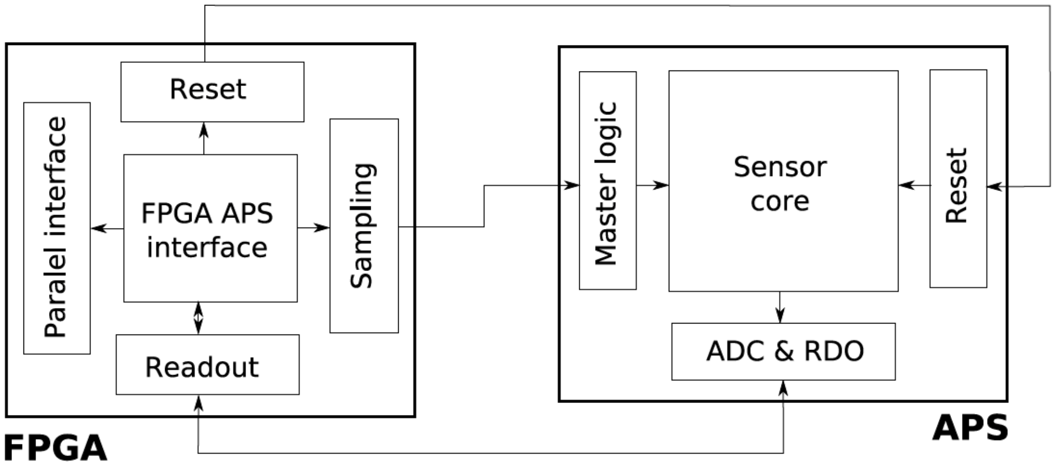

Figure A.3: Block scheme of modules inside the master FPGA and APS and communication between them.

At this moment, design of the new mezzanine board has to be completed. Assembly of the readout system itself can be done thereafter and new modules for the FPGA can be implemented and tuned subsequently. The next step will be matching the existing readout PC utility to current demands and putting the readout system in service. This is the first task of the whole plan. In the second stage, more advanced readout software is planned to be created. Further detectors, such as scintillators, will be added in the next phase to extend testing capabilities.

---

[5] ADC - Analog to Digital Converter

References

[1] L.D. McLerran and B. Svetitsky, Phys. Lett. B**98**, 195 (1981).

[2] J. Kuti, J. Polonyi and K. Szlachanyi, Phys. Lett. B**98**, 199 (1981).

[3] L.D. McLerran and B. Svetitsky, Phys. Rev. D**24**, 450 (1981).

[4] R. Stock, arXiv:0807.1610v1 [nucl-ex], (2008).

[5] BNL-Report, *Hunting the Quark Gluon Plasma*, BNL-73847-2005 (2005).

[6] J. Adams et al.,STAR Collaboration, arXiv:nucl-ex/0501009v3, (2005).

[7] E. Bruna, PhD Thesis, University of Torino, (2007).

[8] J. Dunlop, arXiv:0907.4619v2, (2009).

[9] A.M. Poskanzer, Phys. Rev. C**58**, 1671–1678 (1998).

[10] R. A. Lacey and A. Taranenko, nucl-ex/0610029, (2006).

[11] I. Arsene et al., BRAHMS Collaboration, Phys. Rev. Lett **91**, 072305 (2003).

[12] J.W. Cronin et al., Phys. Rev. D**11**, 3105 (1975).

[13] M. Krůs, Master's Thesis, Czech Technical University in Prague, (2008).

[14] Y. Akiba et al., PHENIX Collaboration, Nucl. Phys. A**774**, 403 (2006).

[15] M. Gazdzicki et al., NA49 Coll., J. Phys. G**30**, 701 (2004).

[16] P. Braun-Munzinger et al., Phys. Lett., B**465**, 15 (1999).

[17] P. Braun-Munzinger, arXiv:nucl-ex/0508024v1, (2005).

[18] W.-M.Yao et al., J. Phys. G**33**, 1 (2006).

[19] H. Evans, conference talk, XXIV Physics in Collision, Boston (2004).

[20] R. Vogt, Eur. Phys. J. ST**155**, 213 (2008).

[21] S.S. Adler et al., PHENIX Collaboration, Phys. Rev. Lett. **94**, 082301 (2005).

[22] J. Adams et al., STAR Collaboration, Phys. Rev. Lett. **94**, 062301 (2005).

[23] B. I. Abelev et al., STAR Collaboration, arXiv:0805.0364, (2008).

[24] Y. L. Dokshitzer, D. E. Kharzeev, Phys. Lett. B**519**, 199 (2001).

[25] N. Armesto et al., Phys. Rev. D**71**, 054027 (2005).

[26] M. Djordjevic et al., Phys. Rev. Lett. **94**, 112301 (2005).

[27] B. I. Abelev, Phys. Rev. Lett. **98**, 192301 (2007).

[28] D. Hornback, arXiv:0804.4825v1, (2008).

[29] NA50 Collaboration, Eur. Phys. J. C**48**, 329 (2006).

[30] k. Prytz, J. Phys. G**19**, 1628 (1993).

[31] S.D. Drell and T.-M. Yan, Phys. Rev. Lett. **25**, 316 (1970).

[32] A.A. Isayev, arXiv:0906.3717v1, (2009).

[33] E. T. Atomssa, arXiv:0907.4787v2, (2009).

[34] M. Harisson et al., Nucl. Instr. and Meth. A**499**, 235 (2003).

[35] K.H. Ackermann et al., Nucl. Instr. and Meth. A**499**, 624 (2003).

[36] M.E. Ileddo, *STAR CDR*, (1992).

[37] W.R. Leo, *Techniques for Nuclear and Particle Physics Experiments*, ISBN 3-540-57280-5, (1994).

[38] M. Anderson, Nucl. Instr. and Meth. A**499**, 659 (2003).

[39] M. Tesař, Bachelor's Thesis, Czech Technical University in Prague, (2008).

[40] D. Beaviset al., STAR Collaboration, *The STAR Heavy Flavor Tracker CDR*, (2009).

[41] L. Arnold, Nucl. Instr. and Meth. A**499**, 652 (2003).

[42] M. Beddo, Nucl. Instr. and Meth. A**499**, 725 (2003).

[43] J. Wu and M. Xu, J. Phys. G**34**, S729 (2007).

[44] P. Fachini, STAR TOF Collaboration, *Proposal for LArge Area Tome of Flight System for STAR*, (2004).

[45] A. Andronic et al., Phys. Lett. B**571**, 36 (2003).

[46] S. H. Lee et al., arXiv: 0709.3637v3, (2008).

[47] E. Bruna et al., Int. J. Mod. Phys. E **16**, 2097 (2007).

[48] J. Kapitan, Eur. Phys. J. C**62**, 217-221 (2009).

[49] R.T. Thew, Nucl. Instr. and Meth. A**610**, 16–19 (2009).

[50] S. Cova et al., Applied Optics **12**, 1956 (1996).

[51] A.N. Otte, PhD Thesis, Technical University Munich (2007).

[52] J. Ninkovic, conference talk, MAGIC Collab. Meeting Munich, (2008).

[53] J. Ninkovic, conference talk, 12th Vienna conf. on Instr., (2010).

[54] J. Ninkovic et al., Nucl. Instr. and Meth. A**610**, 142 (2009).

[55] A. Mathewson et al., Photodetectors and Power Meters SPIE proc. **2022**, 132 (1993).

[56] C. Soldner, Diploma Thesis, Ludwig-Maximilians-University, (2009).

[57] R.L. Aggarwal et al., Solid State Communications **117**, 549 (2001).

[58] Xilinx Spartan-3 FPGA Family Data Sheet, (2009).

[59] Cypress Semiconductor IBIS4-1300 Data Sheet, (2007).